Progress in Oceanography 141 (2016) 60–80

Contents lists available at ScienceDirect

Progress in Oceanography

journal homepage: www.elsevier.com/locate/pocean

Circulation in the Arctic Ocean: Results from a high-resolution coupled ice-sea nested Global-FVCOM and Arctic-FVCOM system

Changsheng Chen [a,b,*], Guoping Gao [b], Yu Zhang [a], Robert C. Beardsley [c], Zhigang Lai [d], Jianhua Qi [a], Huichan Lin [a]

[a] School of Marine Science and Technology, University of Massachusetts-Dartmouth, New Bedford, MA 02744, United States
[b] International Center for Marine Studies, Shanghai Ocean University, Shanghai, PR China
[c] Department of Physical Oceanography, Woods Hole Oceanographic Institution, Woods Hole, MA 02542, United States
[d] School of Marine Sciences, Sun Yat-Sen University, Guangzhou 510275, PR China

ARTICLE INFO

Article history:
Received 29 January 2015
Received in revised form 3 December 2015
Accepted 7 December 2015
Available online 12 December 2015

ABSTRACT

A high-resolution unstructured-grid global-regional nested ice-current coupled FVCOM system was configured for the Arctic Ocean and used to examine the impact of model resolution and geometrical fitting on the basin-coastal scale circulation and transport in the pan-Arctic. With resolving steep bottom slope and irregular coastal geometry, the model was capable of simulating the multi-scale circulation and its spatial variability in the Arctic Basin and flow through the Bering Strait, Fram Strait and Canadian Archipelago. The model-simulated annual-mean velocities were in good agreement with observations within the measurement uncertainty and variability due to insufficient sampling. The errors in the flow direction varied with the flow speed, larger in the weak velocity zone and smaller as the velocity increased. In the upper 50-m layer, the annual-mean circulation pattern was dominated by the wind- and ice-drifting-induced anticyclonic circulation in the Arctic Basin and a relatively strong cyclonic slope current along the edge of the continental shelf. In the deep 200–600-m layer, a relatively permanent cyclonic circulation occurred along the steep bottom slope. These annual-mean circulations accounted for ~85% of the total kinetic energy variance. De-trending the mean flow, an empirical orthogonal function (EOF) analysis showed that the semi-annual and seasonal variability of the sub-tidal flow was dominated by the first and second modes that accounted for ~46% and ~30% of the total variance in the upper 50-m layer and ~58% and 20% in the deep 200–600-m layer. Consistent with observations, the AO-FVCOM-simulated cyclonic slope flow was characterized by a large positive topostrophy. Sensitivity experiment results with various grid configurations suggested that the currents over slopes, narrow straits and water passages featured topographic and baroclinic frontal dynamical scales associated with bathymetric slope and internal Rossby deformation radius. Over the Arctic slope, since these two scales are in the same order, the along-slope current could be captured, as the cross-isobath model resolution was refined to resolve the steep bottom topography. Under this condition, there is no need to add Neptune forcing into the momentum equations. The accuracy of the estimation of the transport through the strait and narrow water passage was affected by the model resolution. In Fram Strait where the flow is characterized by strong lateral current shear resulting from the Atlantic inflow and Arctic outflow, the transport estimation could have a significant uncertainty due to both horizontal and vertical sampling resolutions.

1. Introduction

The circulation in the Arctic Ocean is poorly observed and our present knowledge is based mainly on models (Proshutinsky et al., 2001; Steele et al., 2001; Holloway et al., 2007) that can give insights into the science. The pictures that have emerged from different models are often not consistent and differ substantially in terms of particulars, most notably over the cyclonic flow over steep topographic slopes and the water transport through narrow straits and water passages. Topostrophy, which is defined as $\tau = f(\vec{k} \times \vec{u}) \cdot \nabla D$ (where f is the Coriolis parameter, $\vec{k}$ the unit vector for the vertical axis, $\vec{u}$ the model velocity and D the total depth), was recommended as an indicator to assess the capability of a model to resolve the slope cyclonic flow in the Arctic during the

* Corresponding author at: School of Marine Science and Technology, University of Massachusetts-Dartmouth, New Bedford, MA 02744, United States.
E-mail address: c1chen@umassd.edu (C. Chen).

http://dx.doi.org/10.1016/j.pocean.2015.12.002
0079-6611/

Arctic Ocean Model Intercomparison Project (AOMIP) (Holloway, 2008). Velocity measurements suggested that the Arctic Ocean was characterized by a large positive, significantly time-varying τ, while the τ values produced by most of the Arctic Ocean models were too small in either amplitude or time variability (Holloway and Wang, 2009). Differences in subgrid parameterization were believed to be one cause for the inconsistencies between the model results, since the horizontal resolution in these models were too coarse to resolve steep slope topography (Holloway, 2008). The so-called "Neptune effect", which was specified by a diffusion-based forcing in the form of $-A_H\nabla^2\boldsymbol{u}^*$ (where A_H is the horizontal eddy diffusivity, $\boldsymbol{u}^* = -L^2 f\vec{k}\times\nabla(\log D)$, and L is an eddy length parameter), was recommended to be implemented into the momentum equations for the purpose of improving the representation of the mean flow resulting from eddy-topography interaction (Eby and Holloway, 1994; Holloway and Wang, 2009). In this type of Neptune model, the Neptune flow was depth-independent and can vary with time if the surface elevation is considered in D. A Neptune model did show its capability of improving the simulation of cyclonic slope currents (Holloway and Wang, 2009), which illustrates our views on the importance of subgrid parameterization in the Arctic Ocean under conditions with the present limits in model resolution and computational resources.

The complex geometry of the Arctic coastlines, steep bottom bathymetry along continental slopes and ridges, numerous islands and narrow straits (Fig. 1) has challenged ocean modelling in this basin-scale ocean (Chen et al., 2009). The Arctic Basin is stratified, with a cross-shelf scale defined by an internal Rossby deformation radius of ~6–10 km over the shelf and within narrow straits (Münchow et al., 2007). The Arctic Basin is characterized by an along-slope cyclonic flow with its cross-shelf scale constrained by the width of the steepest slope which is on the order of ~10 km. Over a distance of 10 km over the slope, the water depth could abruptly vary about 1000 m or larger. Driven by astronomical tides, atmospheric forcing at the sea surface, and freshwater discharges from rivers, the spatial structure of the circulation in the Arctic Ocean is highly geometrically-controlled, which requires a state-of-the art model with its horizontal and vertical resolutions capable of resolving complex coastlines, steep continental slopes and strong upper ocean stratification. To satisfy this requirement, the model resolution over the slope and Canadian Archipelago should be of the order of 1/4 of the internal Rossby deformation radius and steepest slope width, which is of the order of ~ 2–3 km.

It is clear that subgrid parameterization depends on model resolution. The Neptune model was developed on an assumption that the model resolution was not sufficient to resolve the slope geometry. As long as the basin-scale circulation was considered, the eddy-topographic interaction should become well resolved as model resolution increased to a level at which the cross-isobath slope of the continental shelf could be realistically represented. Under this condition, the Neptune approach should become unnecessary. Increasing resolution in a model, however, is not a trivial task since it always sacrifices computational efficiency and/or is constrained by computational resources. The surface area of the Arctic Ocean is about 9.0×10^6 km^2. If a structured-grid model with horizontal resolutions of ~1–3 km is used, a total of ~1.0–3.0×10^6 grid cells are required to cover this region. If one uses the quadrilateral grid cells, the total grid cells could be up to ~9×10^6. It is not practical to run such a model for multi-year simulation with limited computational resources.

Grid refinement techniques, such as nesting, conjoined grids and adaptive grids, could be employed to endow Arctic Ocean models with variable resolution capabilities, and to permit these models to better resolve multi-scale processes in global simulations. Either one-way or two-way nesting is a common approach used in both atmosphere and ocean models. The nesting approach needs to enforce mass and energy conservation at the seam where two different-size grids are connected. This approach is, however, fraught with problems. Even if one-way or two-way nesting is used, the structured-grid approach needs to treat mass and energy conservation at the nesting boundary that connects the two different-size grids. In a free-surface shallow-water ocean model, for example, the surface gravity waves are non-dispersive long-waves with phase speed $\sqrt{gD}$. In the discrete form of the finite-difference equations, the model-simulated gravity wave becomes a dispersive wave with a phase speed depending on horizontal resolution ($\sim\sqrt{gD}\sqrt{\frac{\sin^2 k\Delta x+\sin^2 l\Delta y}{(k\Delta x)^2+(l\Delta y)^2}}$, where k and l are the x and y components of the wave number, and Δx and Δy are the x and y components of model grid resolution). Since the grid sizes of the two domains differ at the nesting boundary, the model-computed phase speeds for the same wavelength wave are not equal, so that a special treatment is required to disperse inconsistent-energy from the small domain in order to ensure mass and energy conservation at the nesting boundary. This treatment usually works for a short-term simulation but requires validation for the long-term simulations that are generally done in climate change studies. The unstructured-grid model has the same grid-dependent dispersive phase issue. In the grid generation, a rule of thumb is usually used to avoid a rapid change of the mesh size. For a two-domain nesting problem, however, the unstructured-grid model could link the two domains with common cells. This approach produces the same surface gravity features in the nesting grid zone, which ensures volume and mass conservation on the nesting boundary cells and make this type of model practical to resolve multi-scale processes in the ocean.

We, a joint research team at the University of Massachusetts-Dartmouth (UMASSD) and Woods Hole Oceanographic Institution (WHOI) have developed the unstructured-grid Finite Volume Community Ocean Model (FVCOM) (Chen et al., 2003). The unstructured-grid finite-volume algorithm used in FVCOM combines the advantage of finite-element methods for grid geometric flexibility and finite-difference methods for simple and efficient discrete computation (Chen et al., 2006a, 2006b; Chen et al., 2007). FVCOM solves the flux form of the governing equations in an arbitrary control volume constructed by unstructured triangles with second-order accurate discrete flux schemes. This numerical approach provides an accurate presentation of local mass, heat and salt conservation. FVCOM was originally designed for regional, coastal and estuarine problems with complex irregular geometry. Flexibility of the triangular grid allowed us to design the model grid to be consistent with physical scales; higher resolution over the steep bottom topography along continental margins and narrow water passages and coarser resolution in the interior, to accurately simulate slope fronts and currents in basin-scale applications.

We have used FVCOM to configure an Arctic Ocean model (hereafter referred to as AO-FVCOM). With various grid configurations, this unstructured-grid model provided us a tool to examine the influence of geometric fitting and model resolution on the simulation results of the circulation in the Arctic and water transport through Bering and Fram Straits as well as the Canadian Arctic Archipelago (CAA). There are many Arctic Ocean models that have provided various results for the Arctic circulation. To our knowledge, however, only a few analyses have been conducted to examine how model performance is affected by how well the geometric details are fitted over slopes and in complex coastal regions. It is clear that we need a higher resolution model for the Arctic. However, it is unclear what is the resolution required to resolve the slope currents and the spatial variation of the flow through narrow

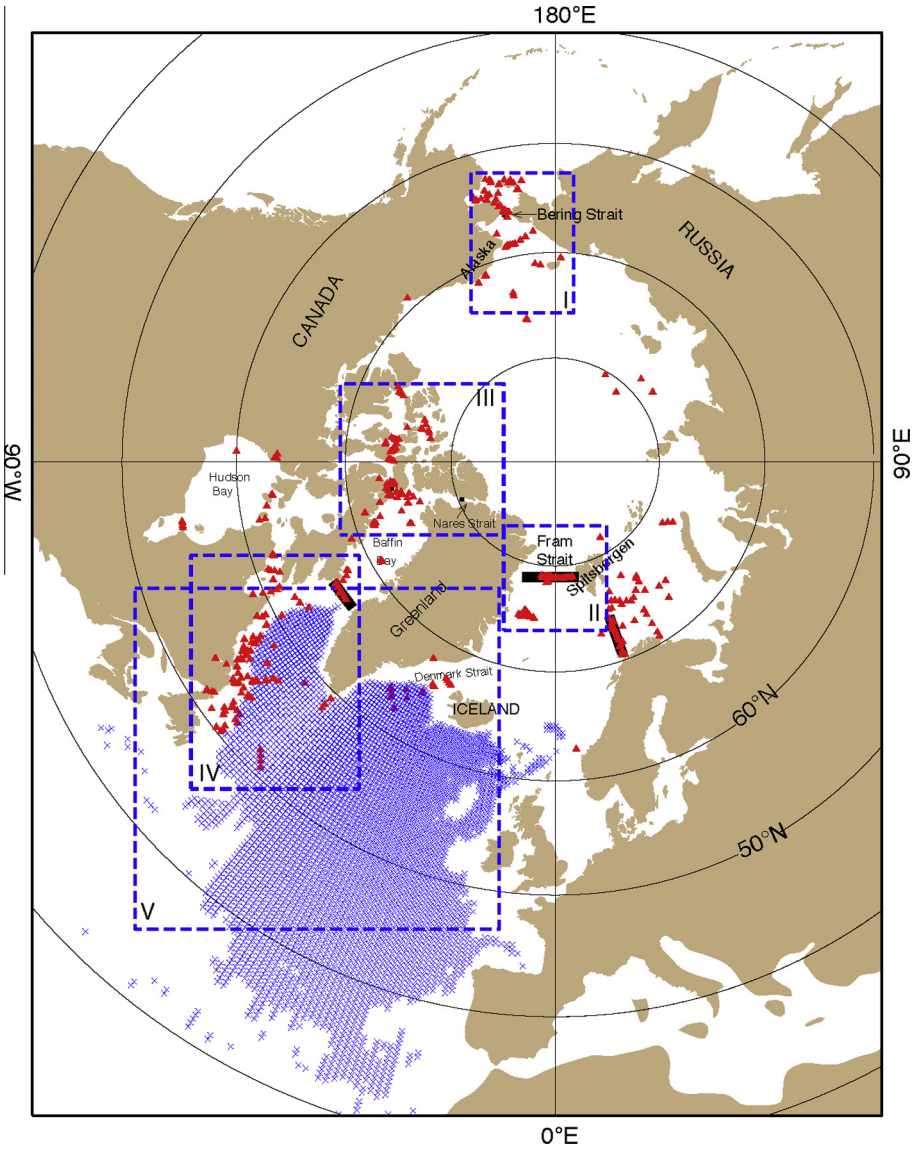

Fig. 1. Geometry of the Arctic and adjacent North Atlantic and Pacific Oceans and locations of current measurements divided into five regions: I: the Bering Sea; II: Fram Strait; III: Canadian Archipelago; IV: the Greenland and Labrador Sea shelf and V: the North Atlantic Ocean/Greenland Sea. Red up-triangular symbols: mooring sites; blue cross symbols: sites where the mean velocity was calculated by box-averaging float trajectory records; and black heavy lines: the sections where transport was estimated based on current measurements. (For interpretation of the references to colour in this figure legend, the reader is referred to the web version of this article.)

straits. Within the known circulation scale, how does a model perform as the model horizontal resolution changes? If one defines the grid resolution as the numerical scale, what level of unreality could occur in the model simulation when its numerical scale does not match with the physical scale? For the Arctic Ocean, these questions could be addressed by comparing the flow spatial structures, including the location and intensity of the flow over the slope in the Arctic and complex geometrically featured narrow straits and water passages through the CAA. They are also better addressed based on climatological conditions, which help us distinguish the spatial variability from the temporal variability.

In this paper, we attempt to assess the performance of AO-FVCOM under climatologically averaged conditions. The model-data comparison was made with an aim at evaluating the capability of AO-FVCOM to resolve the spatial variation of the multi-scale circulation patterns in the Arctic and CAA and to provide a statistically meaningful error analysis. Particular attention was paid to requisite resolutions to resolve the cyclonic flow over steep slopes that are characterized by a large positive, time-varying topostrophy. Running the AO-FVCOM with various horizontal resolutions, we also examined the dynamics involving grid refinement with support from previous theoretical studies.

Remaining sections of this paper are organized as follows. In Section 2, the AO-FVCOM and the design of the numerical experiments are described. In Section 3, results of model simulation under climatological forcing conditions are presented and compared with observations. In Section 4, the impacts of grid resolution on the slope currents and topostrophy are discussed and an empirical orthogonal analysis (EOF) is conducted to characterize the key features of the cyclonic flow over the Arctic slope. In Section 5, the conclusions are summarized.

2. AO-FVCOM/Global-FVCOM and design of numerical experiments

The AO-FVCOM was developed under the spherical coordinate framework of FVCOM. FVCOM is a prognostic, unstructured-grid, Finite-Volume, free-surface, 3-D primitive equation Community

Ocean Model (Chen et al., 2003, 2006a, 2006b, 2007, 2013). The equations are cast in a generalized terrain-following coordinate system with spatially variable vertical distribution (Chen et al., 2013). In the horizontal, the equations are discretized using non-overlapped triangular grids, which provide accurate fitting of irregular coastal geometries and flexibility in refining the grid over steep continental margins, ridges, and around islands. The spatial fluxes of momentum are discretized using a second-order accurate finite-volume upwind method (Kobayashi et al., 1999). A flux formulation for scalars (e.g. temperature, salinity) is used in conjunction with a vertical velocity adjustment to enforce exact conservation of the scalar quantities. A Smagorinsky formulation (Smagorinsky, 1963) is used to parameterize horizontal diffusion and turbulent vertical mixing is calculated using the General Ocean Turbulence Model (GOTM) libraries (Burchard, 2002), with the 2.5 level Mellor and Yamada (1982) turbulence model used as the default.

The AO-FVCOM is a regional model nested with Global-FVCOM. In this study, the model was configured with three regional grids with finest horizontal resolutions of 8.0, 2.0 and 0.5 km (hereafter referred to as Grid-I, Grid-II and Grid-III) (Fig. 2). An example of these three grids over the Beaufort Sea shelf along Alaska is shown in Fig. 3. These three grids contained 86,497, 233,003, and 1,068,117 elements, respectively, with the resolution distributions shown in Fig. 4. The number of cells with a resolution of ~1.0 km or less in Grid-III was $\sim 1.2 \times 10^5$ more than the total cell number in Grid-II. A hybrid terrain-following coordinate was used in the vertical, with a total of 45 layers. In regions deeper than 225 m, the s-coordinate was used, with 10 and 5 uniform layers near the surface and bottom, respectively. The σ-coordinate was used in the shallow continental and coastal regions shallower than 225 m, with the transition between the two coordinates located along the 225-m isobath at which the thickness of all layers was 5 m. This hybrid coordinate prevented numerical errors in the simulation of the surface mixed layer and bottom boundary layer dynamics in the interior without losing vertical resolution in the shallower coastal regions.

The AO-FVCOM was run with the boundary conditions provided by the Global-FVCOM through a one-way nesting approach. The AO-FVCOM shared the same common grid cells with Global-FVCOM in its boundary zones. The nesting boundary zone consisted of cells connected to two boundary lines through triangular nodes. We first ran the Global-FVCOM and output all variables on the nesting boundary cells (nodes and centroid) at every time step, and use this output as the boundary condition to drive AO-FVCOM. The Global-FVCOM covered the entire global ocean with inclusion of all major rivers. It had a horizontal resolution of 2 km (in the coastal regions) to 50 km (in the interior). Global-FVCOM used the same hybrid coordinate as AO-FVCOM and shared the same common grids over a transition zone connected to the nesting boundary. Both AO-FVCOM and Global-FVCOM were fully coupled with the unstructured-grid sea ice model implemented based on the Los Alamos Community Ice Code (hereafter referred to as UG-CICE) (Hunke and Lipscomb, 2006; Gao et al., 2011). The Global-FVCOM was driven by (a) astronomical tidal forcing with eight constituents (M_2, S_2, N_2, K_2, K_1, P_1, O_1 and Q_1), (b) surface wind stress, (c) net heat flux at the surface plus shortwave irradiance in the water column, (d) surface air pressure gradients, (e) precipitation (P) minus evaporation (E), and (f) river discharges. The model included 406 river inputs around the coast. The daily records from USGS measurement sites (source: http://www/usgs.-gov and www.ec.gc.ca) were used to calculate the daily climatologic river discharge rates along the US and Canadian coasts, while the freshwater outflow data used for other rivers were from the global river inflow climatology used in Global Navy Coastal Ocean Model (GNCOM) (Barron and Smedstad, 2002), with an update of the direct measurement records collecting from our international collaborators. The initial condition of temperature and salinity in the model was specified using the January global climatologic fields, in which the Arctic Ocean region was constructed using the Polar Science Center Hydrographic climatology (PHC3.0) (Steele et al., 2001).

In Gao et al. (2011), the AO-FVCOM ran with climatological forcing conditions, in which the climatology referred to the meteoro-

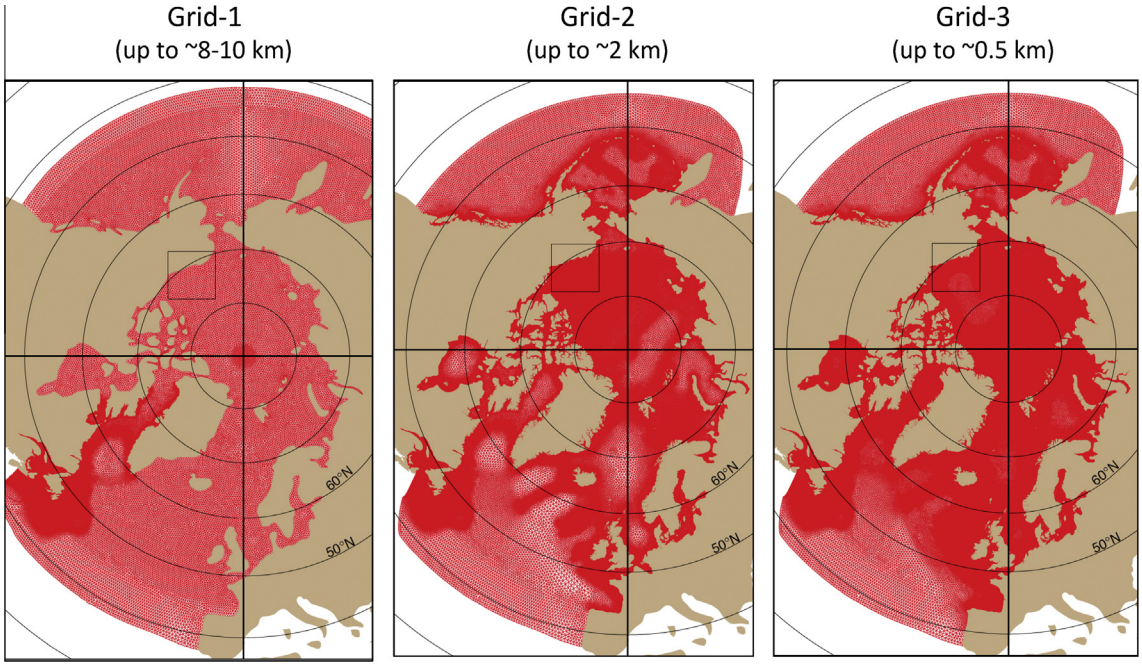

Fig. 2. Unstructured triangular meshes of AO-FVCOM for the Grid-I (left), Grid-II (middle) and Grid-III (right) cases. The finest horizontal resolution was ~8–10 km, ~2 km and ~0.5 km for these three cases, respectively. The Grid-I and Grid-II AO-FVCOMs were merged with Global-FVCOM and run without using the nesting approach. The Grid-III AO-FVCOM was run through one-way nesting with Global-FVCOM. A box shown in each figure is the region for an enlarged view shown in Fig. 3.

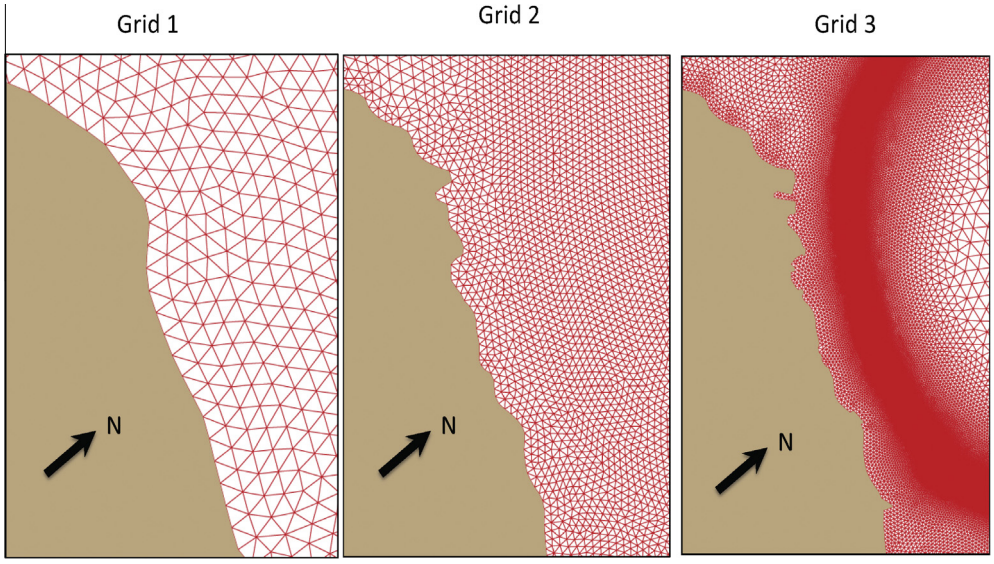

Fig. 3. Enlarged views of the unstructured triangular meshes over the Alaska shelf for the Grid-I (left), Grid-II (middle) and Grid-III (right) cases. The horizontal resolutions over this shelf were up to ~20–30 km, ~8–10 km and ~1 km for these three cases, respectively. An arrow with "N" indicates the direction to the North Pole.

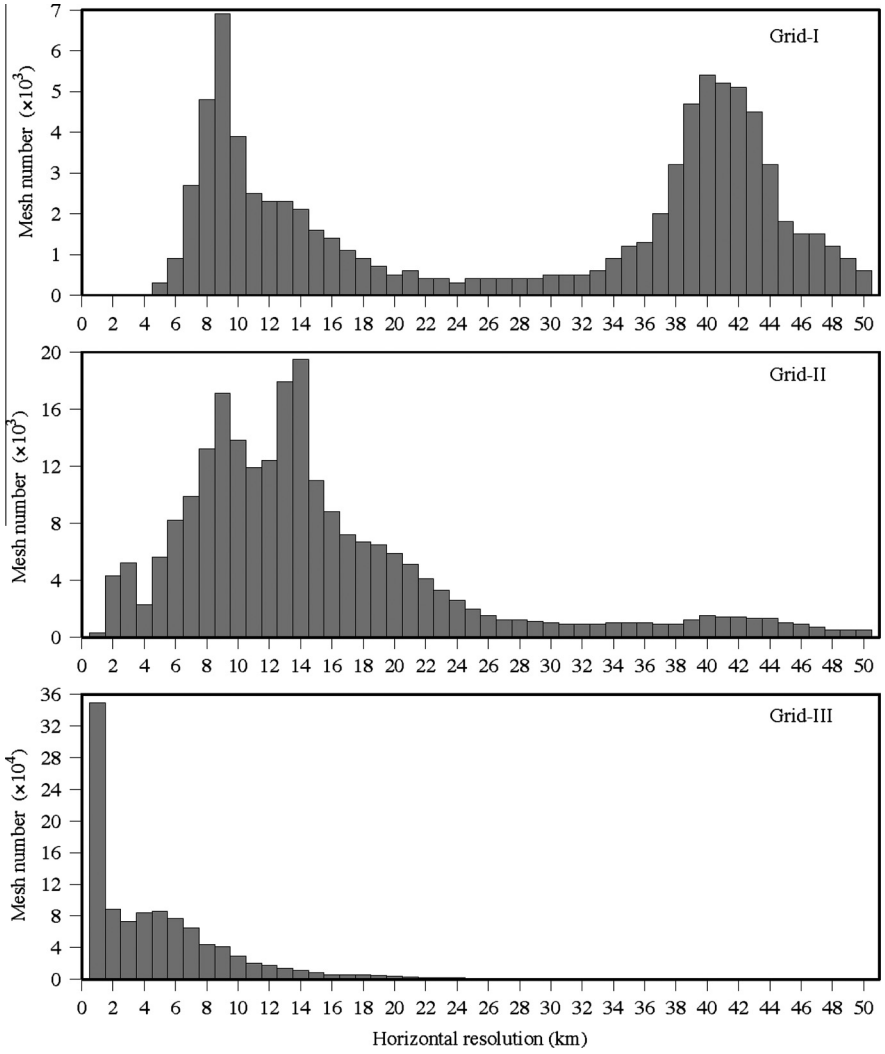

Fig. 4. Distribution of the mesh number versus the grid resolution for the Grid-I (top), Grid-II (middle) and Grid-III (bottom) cases.

logical forcing derived from the European Center for Medium Range Weather Forecast (ECMWF) reanalysis ERA 15 over 1978–1994, with daily surface wind stress, net heat flux plus short wave irradiance, precipitation minus evaporation, surface air temperature and pressure [source: Ocean Modeling Intercomparison Project (OMIP at website addressed http://www.omip.zmaw.de)]. In order to avoid the artificial effect due to the open boundary condition, the AO-FVCOM grid was merged into the Global-FVCOM and ran as a single-grid Global-FVCOM model for a 50-year spin up. The 50-year spin-up was determined based on the 1-D ice simulation result, which showed that for the given climatological daily heat flux, it took ~50 years for the ice thickness to reach an equilibrium state (Gao, 2011). Gao et al. (2011) extended the 1-D experiment to a 3-D case with realistic Arctic geometry and found that given a spatially-uniform ice condition at start up, it took more than 40 years for the Global-FVCOM-simulated ice extent and thickness to reach an equilibrium state. This was the reason we spin up the Global-FVCOM for 50 years and then defined the model equilibrium state solution as the climatological field. In Gao et al. (2011), the Global-FVCOM ran with the inclusion of data assimilation of the monthly climatological temperature/salinity (*T*/*S*) fields. The model-simulated temperature and salinity were adjusted through an optimal interpolation (OI) data assimilation to ensure the model-predicted monthly mean *T*/*S* remain close to the monthly climatological temperature and salinity for the long-term simulation. The assimilation only adjusted the monthly mean *T*/*S*, with no influences on the model-produced hourly and daily temporal and spatial variations.

Initialized with a 50-year spin-up field produced by Gao et al. (2011), we ran the Global-FVCOM with the Grid-I grid in the Arctic for a time period of 1978–2014. To be consistent with this long-term simulation, we have updated the "climatological forcing" using the atmospheric field produced by the daily averaged product of version-2 dataset for the Common Ocean ice Reference Experiments (CORE-v2) for the period 1978–2009 and the National Center for Environment Prediction and the National Center for Atmospheric Research (NCEP/NCAR) for the period 2010–2014, and conducted our experiments here through the following two steps.

Step 1: We re-ran Global-FVCOM with the new climatological atmospheric forcing produced using the 37-year (1978–2014) averaged daily meteorological fields for an additional 7 years with assimilation with the monthly mean *T*/*S* fields. The initial conditions for ice, temperature, salinity and velocity were specified using the 50-year spin-up field produced by Gao et al. (2011). By using the 50-year spin-up field (the ice has already reached an equilibrium state), we found that both ice and flow fields reached an equilibrium state over a period of 5 years, so that a 7-year simulation was long enough for the climatologically based studies carried out in this paper. We output all variables on the nesting boundary cells (at triangle nodes and centroids) at every time step over the 7-year simulation period to build the nesting boundary forcing for the AO-FVCOM.
Step 2: we used the same climatologically atmospheric forcing to drive the Grid-I, Grid-II and Grid-III AO-FVCOM models with an initial condition output from the Global-FVCOM output at 00:00:00 January 1 and boundary conditions specified using the Global-FVCOM model output on the nesting boundary cells. The integration was repeated periodically over an annual basis for 7 years with no data assimilation. A quasi-equilibrium state was reached after 5 years' of integrations and the daily output from year 7 year was used as the climatological model fields for the model-data comparison.

The Global-FVCOM ran with a time step of 300 s. It took a 24-h computational time on 24 nodes (×8 CPU processors) Linux clusters to run the Global-FVCOM (merged with the Grid-I AO-FVCOM grid) for a one-year simulation. Since the shortest length of the smallest triangle was about 2 km in the Global-FVCOM, it was not required to reduce the time step when we ran the AO-FVCOM for the Grid-I and Grid-II cases. In the Grid-III case, the minimum length of the smallest triangle was about 200–300 m, so that we needed to reduce the time step to 80 s.

The AO-FVCOM was validated for tidal simulation in Chen et al. (2009). Gao et al. (2011) compared the model-simulated and observed ice extents, concentrations and drift velocities over the time period of 1979–1994. In this paper, we will focus on the comparison with observed currents. We collected all available current, surface drifter and float data in the Arctic and adjacent oceans (Table 1, Fig. 1) and used them to validate AO-FVCOM in five regions defined here as (I) Bering Strait, (II) Fram Strait, (III) Canadian Archipelago, (IV) Greenland and Labrador Sea shelf, and (V) the North Atlantic Ocean/Greenland Sea. The length of the record for each data set is given in Table 1, which varies over a time range of a month to a year. The comparisons were made for the annually averaged fields, with focus on spatial distribution, speeds and directions of the currents at measurement depths. To quantify the critical need of model resolution and geometrically resolving, we have run AO-FVCOM with Grid-I, Grid-II and Grid-III configurations under the same forcing conditions. We first compared Grid-I

Table 1
Data sources used for the model-data comparison.

Dataset or section names	Periods	Source
Bering Strait	1990–2008	http://arcss.colorado.edu/arcss/intro.html
Chukchi data sets	10/1990–10/1991	http://arcss.colorado.edu/arcss/intro.html
Chukchi datasets (SBI)	07/2002–09/2004	http://arcss.colorado.edu/arcss/intro.html
Chukchi borderlands	08/2002–09/2002	http://arcss.colorado.edu/arcss/intro.html
Lomonosov Ridge and Eurasian continent	08/1995–09/1996	http://arcss.colorado.edu/arcss/intro.html
Fram Strait	04/1991–05/2002	http://nsidc.org/data/g02139.html
North pole environmental observatory data	03/2001–04/2008	http://www.eol.ucar.edu/projects/arcss/
Lancaster Sound/Barrow Strait	1981,1984 1999–2008	http://www.mar.dfo-mpo.gc.ca/science/ocean/seaice/data_e.html
Cardigan Strait	1999–2008	http://www.mar.dfo-mpo.gc.ca/science/ocean/seaice/arctic_e.html
Nares Strait	07/2003–09/2007	http://www.udel.edu/CATS/healy_2007/expedition/index.html
Davis Strait	9/1987–9/1990 2004–2007	http://www.mar.dfo-mpo.gc.ca/science/ocean/database/data_query.html http://iop.apl.washington.edu/projects/ds/html/overview.html
Hudson Strait		Fiamma Straneo at WHOI
Barents Sea Opening	08/1997–08/2001	Ingvaldsen et al. (2004)
The Irmingar Sea	1986–1991	Dickson and Brown (1994)
700-m subsurface floats	11/1994–07/2002	Kara L. Lavender, W. Brechner Owens and Russ E. Davis from WHOI

and Grid-II results with observed currents, and then examined how sensitive the model-simulated currents was to the model resolution as different grids were used.

3. Model-data comparisons

In region I – the Bering Sea-Bering Strait-the Alaska coast, AO-FVCOM captured the spatial distribution of subtidal currents (Fig. 5). The model showed that the Pacific Ocean water flowed around St. Lawrence Island and entered Bering Strait. The inflow of Bering Strait produced a northward current over the Chukchi Shelf and then separated into three branches: (1) a coastal current along the Alaska coast towards Barrow Canyon, (2) a northwestward current towards Herald Canyon, and (3) a relatively weak middle branch towards Hanna Trough. This last branch turned clockwise to join the Alaska Coastal Current. The model-predicted flow patterns were not only consistent with the local circulation schematized from limited observations (Coachman et al., 1975; Roach et al., 1995; Weingartner et al., 1998, 2005), but also magnitude, direction and spatial variability of the flow matched reasonably well with observations at measurement sites (Fig. 5). We calculated the statistics of the model-data comparison results

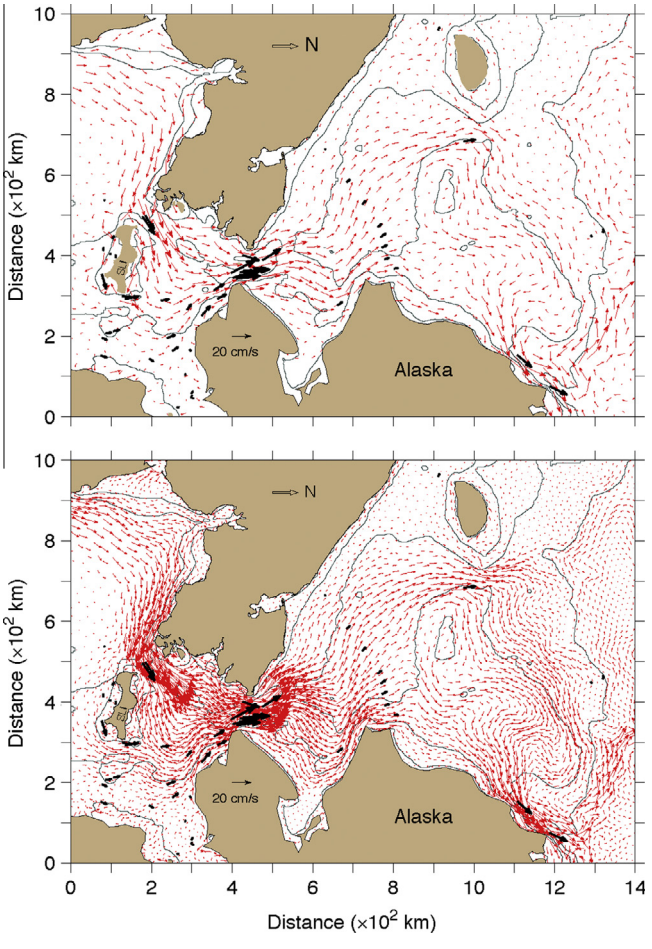

Fig. 5. Model-predicted annual-mean currents (red vectors) averaged over the upper 50-m water column in Bering Strait for the Grid-I (upper) and Grid-II (lower) cases. The observed velocities (black vectors) averaged annually and through the upper 50 m (when the multi-depth measurements were made) are superposed on the model field. The velocity vectors displayed in the Grid-II case are spaced every 15-km apart. These panels are oriented with West pointing upward. SLI: St. Lawrence Island. The arrow with "N" indicates the direction to the North Pole. (For interpretation of the references to colour in this figure legend, the reader is referred to the web version of this article.)

Table 2
Bering Strait and Beaufort Sea Shelf. Statistics for the speed (S) and direction (θ) differences (ΔS, $\Delta\theta$) for observed and model-simulated velocities. The number of current measurements used in this comparison is 177. Statistics for the angle difference were estimated only for the measurements with velocity $\geqslant$3.0 cm/s. Subscripts "o" and "m" denote "observed" and "model-simulated".

Velocity	Mean (cm/s)	STD (cm/s)	Max (cm/s)	Min (cm/s)
S_o	9.80	8.87	34.18	0.45
S_m	12.89	13.55	45.48	0.57
	Mean (cm/s)	RMSE (cm/s)	Max (cm/s)	Min (cm/s)
ΔS	5.28	6.38	28.55	0.03
Angle error	Mean	RMSE	Max	Min
$\Delta\theta$	14.96°	13.71°	53.53°	0.50°

based on 177 measurements in the upper 50 m in this region. The mean values of the difference were 5.3 cm/s in speed and 15.0° in direction (Table 2). The mean speed error accounted for 15.5% of the maximum observed velocity. The observations used in this comparison were either from a single time series record or multiple time series records in different years. At a site where multiple year records were available, the variability of the mean current averaged over different datasets can be up to 5.0 cm/s. Considering this variability, the model was robust to capture the observed flow in this region.

With reasonable matching of coastal geometry and resolving of islands, the model-simulated flows for Grid-I and Grid-II cases exhibited the same spatial pattern. As horizontal resolution was increased, the model-data comparison around St. Lawrence Island was significantly improved. The flow speed on the western shelf of the island was remarkably overestimated in the Grid-I case, while it was well reproduced in the Grid-II case. In the northern coastal region of Alaska characterized by a large concave shoreline, the Grid-II case provided a better resolution of the slope area of the continental shelf. As a result, the maximum along-isobath flow shifted offshore towards the shelf break, which resulted in a weaker flow in the shelf region in the Grid-II case than in the Grid-I case. We will discuss this more in Section 4.

The model-predicted volume transports through Bering Strait were 1.23, 0.95 and 0.78 Sv for the cases with Grid-I, Grid-II and Grid-III, respectively (Table 3). The raw bathymetric data available

Table 3
Volume and freshwater fluxes through Bering Strait.

Sources	Volume flux (Sv)	Freshwater flux (mSv)	Comments
AO-FVCOM (Grid I-30 km)	1.23	87.95	1978–1994 climatology
AO-FVCOM (Grid-II: 7 km)	0.95	65.98	1978–1994 climatology
AO-FVCOM (Grid-III: 3 km)	0.78	59.64	1978–1994 climatology
Coachman and Aagaard (1988)	0.8		1976–1977 reanalysis
Aagaard and Carmack (1989)		53	
Roach et al. (1995)	0.83 ± 0.25		Sep. 1990–Sep. 1994
Woodgate and Aagaard (2005)	0.8	76 ± 10	1990–2004
Woodgate et al. (2006)	0.7–1.0	41.22 (2001) 66.59 (2004)	1990–2004
Clement et al. (2005)	0.65 ± 0.25	47	Navy-model, 1979–2001
Woodgate et al. (2010)	0.6–1.0		1991–2007

Note: The number within brackets in the top three rows is the finest resolution in the AO-FVCOM in Bering Strait.

in the strait had a spatial resolution of ~3 km. The transport value obtained for these three cases represented a bathymetry-depending solution. As the model grid horizontal resolution was about 7 km in the Grid-II case or higher in the Grid-III case, the model-predicted transport was in the measured range of 0.7–1.0 Sv (Roach et al., 1995; Woodgate and Aagaard, 2005; Woodgate et al., 2005a, 2005b, 2006, 2010). This value was also consistent with previous re-analysis and model results (Coachman and Aagaard, 1988; Clement et al., 2005). The freshwater flux was defined as a salinity transport relative to a reference salinity of S_{ref} = 34.8 in the form of

$$\mathrm{FWT} = \left\langle \iint u_n[S_{ref} - S(x,y,z,t)]/S_{ref}\,dA \right\rangle \quad (1)$$

where u_n is the current velocity normal to the section area A across the strait and the sign "$\langle\ \rangle$" indicates the annual mean. The model-computed freshwater flux was 87.95 mSv for Grid-I, 65.98 mSv for Grid-II and 59.64 mSv for Grid-III (Table 3). Dividing the freshwater flux by the volume flux, we found that the difference of the averaged value of $(S_{ref} - S)/S_{ref}$ for these three cases was in a range of ~9%. Therefore, a difference of up to ~32% in the freshwater flux for Grid-I and Grid-III was mainly caused by the difference in the volume flux, which was up to ~43% between the Grid-I and Grid-III cases. The Grid-III model-computed freshwater flux was in the range of 41–76 ± 10 mSv reported by previous investigators listed in Table 3.

Region II-Fram Strait is characterized by the Arctic outflow along the Greenland coast and the North Atlantic inflow around Svalbard. AO-FVCOM was capable of resolving these two flows (Fig. 6). The Arctic water flowed out of Fram Strait with a main stream of up to 20.0 cm/s along and nearby the Greenland slope. The North Atlantic slope water moved northwestward along the slope from the Norway coast and entered Fram Strait along the western shelf of Svalbard. This slope water mass split into two branches along a bifurcation terrain: (1) one flowing continuously northward along the slope and entering the Eurasian Basin, and (2) the other moving along the slope of an offshore-extended submerged plateau and then turning cyclonically to join the Arctic outflow over the Greenland slope. The model also produced a cross-strait flow in the upstream area of the bifurcation terrain, where the inflow had a similar speed as the outflow. The model-produced flows were in good agreement with currents recorded at current meter moorings (Fahrbach et al., 2001; Schauer et al., 2004): the observed mean flow coincided in direction and magnitude with the model-computed flow, even for a cyclonically turned cross-strait flow (Fig. 6). We calculated the statistics of the model-data comparison results based on 83 measurements available in the upper 75 m of this region, and the results showed that the mean values of the difference were 2.3 cm/s in speed and 13.9° in direction (Table 4). The mean speed error accounted for 10.4% of the maximum observed velocity. At a site where multiple year records were available, the observed current variability can be up to 7.8 cm/s. Considering that the model simulation was run with climatological forcing, while in situ current measurements were made in different time periods with various record lengths, it was not surprising that the measured current variability is larger than the model-data difference.

Similar to Region-I, as the horizontal resolution was increased, the main streams of inflow and outflow shifted towards to the shelf break, along with narrowing of their cross-isobath widths. Correspondingly, the along-isobath Atlantic inflow was intensified over the slope, especially along the slope of the offshore-extended submerged plateau off Svalbard. In addition to appearances of geometrically relevant mesoscale recirculation eddies off the slope and over the continental shelf, a well-defined coastal outflow jet

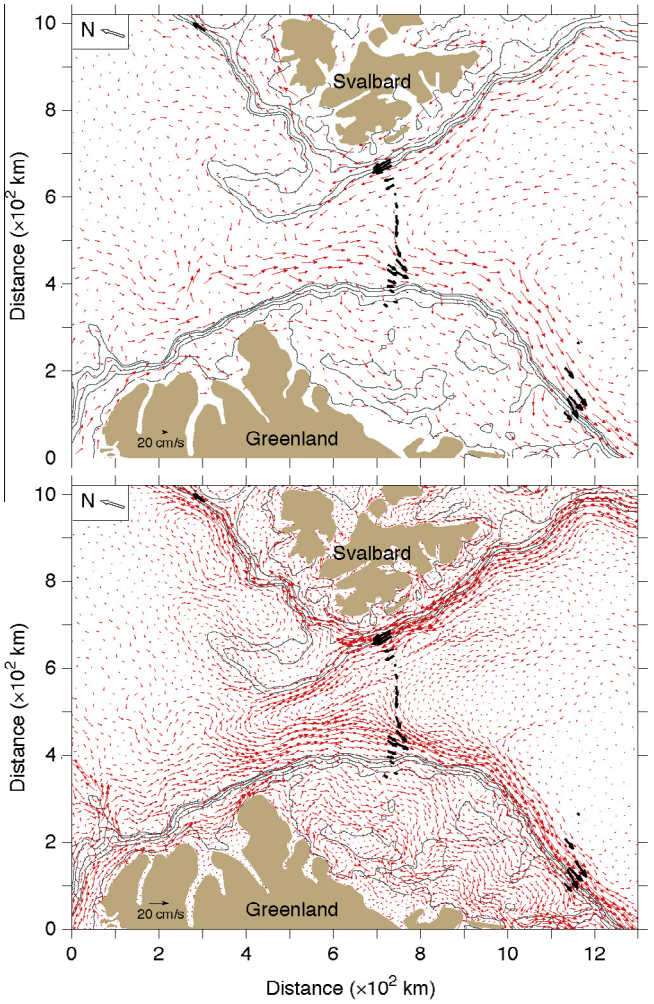

Fig. 6. Model-predicted annual-mean currents (red vectors) averaged over the upper 50-m water column in Fram Strait and adjacent regions for the Grid-I (upper) and Grid-II (lower) cases. The observed velocities (black vectors) averaged annually and through the upper 50 m (when the multi-depth measurements were made) are superposed on the model field. The velocity vectors displayed in the Grid-II case are spaced every 15-km apart. These panels are oriented with East pointing upward. The arrow with "N" indicates the direction to the North Pole. (For interpretation of the references to colour in this figure legend, the reader is referred to the web version of this article.)

Table 4
Fram Strait. Statistics for the speed (S) and direction (θ) differences (ΔS, $\Delta\theta$) for observed and model-simulated velocities. The number of current measurements used in this comparison is 87. Subscripts "o" and "m" denote "observed" and "model-simulated".

Velocity	Mean (cm/s)	STD (cm/s)	Max (cm/s)	Min (cm/s)
S_o	10.88	6.22	22.15	1.14
S_m	10.37	7.24	22.51	0.15
	Mean (cm/s)	RMSE (cm/s)	Max (cm/s)	Min (cm/s)
ΔS	2.32	2.19	8.10	0.03
Angle error	Mean	RMSE	Max	Min
$\Delta\theta$	13.88°	11.53°	57.25°	1.92°

appeared along the inner shelf of Greenland. It was clear that the flow direction was highly controlled by local bathymetry, which was better resolved in the refined Grid-II case.

In this inflow-outflow strait, as a result of significant changes in the flow field with model grid resolution, a simple monotonically

convergence solution of the volume flux did not appear for the cases of Grid-I, Grid-II and Grid-III. The model-computed net outflow volume flux was 3.3 Sv for Grid-I, 1.4 Sv for Grid-II and 2.1 Sv for Grid-III (Table 5). The results for Grid-II and Grid-III were similar to the values of 1.7–1.9 Sv predicted by the OPYC model (Holland and Mysak, 1996; Karcher and Oberhuber, 2002) and 2.3 Sv predicted by the POP model (Maslowski et al., 2004). The net outflow volume flux estimates varied over a large range from 1.7 Sv (Rudels et al., 2008; Rudels, 2011) based on geostrophic calculation to 2.0 ± 2.7 Sv (Schauer et al., 2008) and 4.2 ± 2.3 (Fahrbach et al., 2001) from direct current measurements. Taking the measurement uncertainty into account, the AO-FVCOM results for the three cases were all in reasonable agreement with observations. The AO-FVCOM-computed net freshwater outflow flux was in the range of 64.8–78.4 mSv, which is similar to the range of 65.0–95.0 mSv estimated from ^{18}O measurements (Meredith et al., 2001) and the NAOSIM model (Karcher et al., 2005). Significantly lower values of 28.0 mSV and 32.0 mSv were reported based on hydrographic data (Aagaard and Carmack, 1989) and mooring-based estimates (Holfort and Hansen, 2004). Since no volume flux data were provided, it was difficult to judge what led to such a lower net freshwater outflow flux. The simulations with Grid-I, Grid-II and Grid-III also suggested that the uncertainty in the net volume flux estimation across this strait could be large if the spatial sampling resolution was not sufficient to resolve the cross-strait shear of the inflow and outflow.

In both Bering and Fram Straits, although the mean value of the difference between model-simulated and observed velocities was within the flow variability due to insufficient sampling, the speed difference varied in a large range from 0.1% to 83.6% in Bering Strait and from 0.1% to 36.6% in Fram Strait. The maximum direction difference exceeded 53.5° in Bering Strait and was up to 57.3° in Fram Strait. In these two strait regions, the model-simulated flow moved parallel to local isobaths, which were consistent with observations. The direction error varied with the flow speed, with the largest values occurring in the speed regime of <5 cm/s and smaller values as the speed increased (Fig. 7). The error distribution with respect to the observed flow speed was fitted well by the square-power regression function with an r^2 value of 0.97 (r: correlation coefficient) and a RMSE of 6.6° at a 95% confidence level. This distribution was consistent with measurement uncertainties: a small error in the weakly flow regime could lead to a big error in the flow direction.

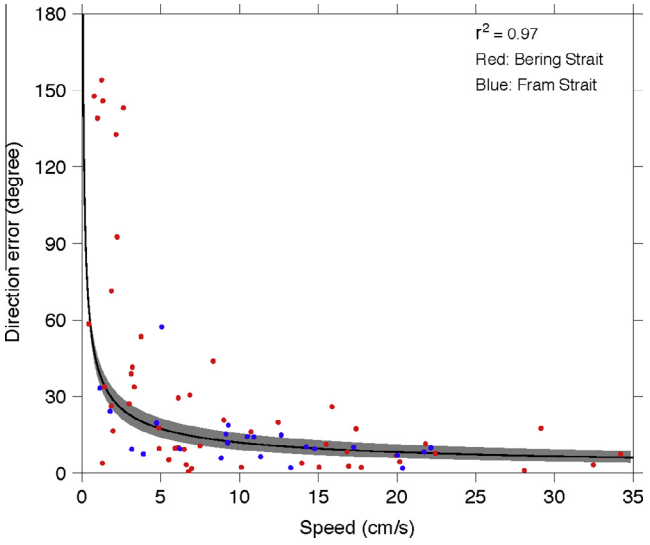

Fig. 7. Distribution of the velocity direction error versus the observed velocity magnitude for the comparison shown in Figs. 5 and 6. Black line: the regression fitting curve with a correlation coefficient of r^2 = 0.97 and RMSE = 6.6°; gray shaded area: the 95% confidence bounds of the power fitting. The fitting was done using the Matlab cftool.

Region III – The Canadian Archipelago is characterized by numerous islands and narrow passages that are not resolved in many current global ocean models. For example, Nares Strait is one of the major water passages to transport low-salinity water from the Arctic to the western North Atlantic Ocean. The observed current in this strait was characterized by a southward coastal jet with the cross-strait scale defined by an internal Rossby deformation radius (R_I) of ~9.6 km (Münchow et al., 2007). This means that in order to resolve the southward coastal jet, the model requires a cross-strait resolution much less than the internal Rossby deformation radius. Failure to resolve this scale could lead to a wrong cross-shelf distribution of the southward flow in the model simulation. An example of this is illustrated in Fig. 8, which shows the distributions of current vectors averaged throughout the upper 50-m water column for the Grid-I and Grid-II cases. The Grid-II case had a horizontal resolution of ~2 km (~0.2 R_I) in Nares Strait. In this case, facing to the flow direction, the current in the segment

Table 5
Volume and freshwater fluxes through Fram Strait.

Sources	Volume flux (Sv)	Freshwater flux (mSv)	Comments
AO-FVCOM (Grid-I: 30 km)	3.3	70.2	1978–1994 climatology
AO-FVCOM (Grid-II: 10 km)	1.4	78.4	1978–1994 climatology
AO-FVCOM (Grid-III: 4 km)	2.1	64.8	1978–1994 climatology
Aagaard and Carmack (1989)		28.0	Hydrographic data estimates
Holland and Mysak (1996)	1.7		OPYC model
Meredith et al. (2001)		63.0–95.0	^{18}O measurements Aug–Sept, 1997,1998
Fahrbach et al. (2001)	4.2 ± 2.3		Sept. 1997–Sept. 1999
Karcher and Oberhuber (2002)	1.9		Climatology-OPYC model
Maslowski et al. (2004)	2.3		Climatology-POP model
Schauer et al. (2004)	2.0–4.0 ± 2.0		Sept. 1997 to Aug. 2000
Holfort and Hansen (2004)		32.0	Mooring-based estimates
Karcher et al. (2005)		78.0 (1990) 65.0 (1948–2002)	NAOSIM model
Dickson et al. (2007)		65.0–95.0	
Schauer et al. (2008)	2.0 ± 2.7		1997–2006
Rudels et al. (2008)	1.7	65.0	Geostrophy (1980–2005)

Note: The number within brackets in the top three rows is the finest resolution in the AO-FVCOM in Fram Strait.

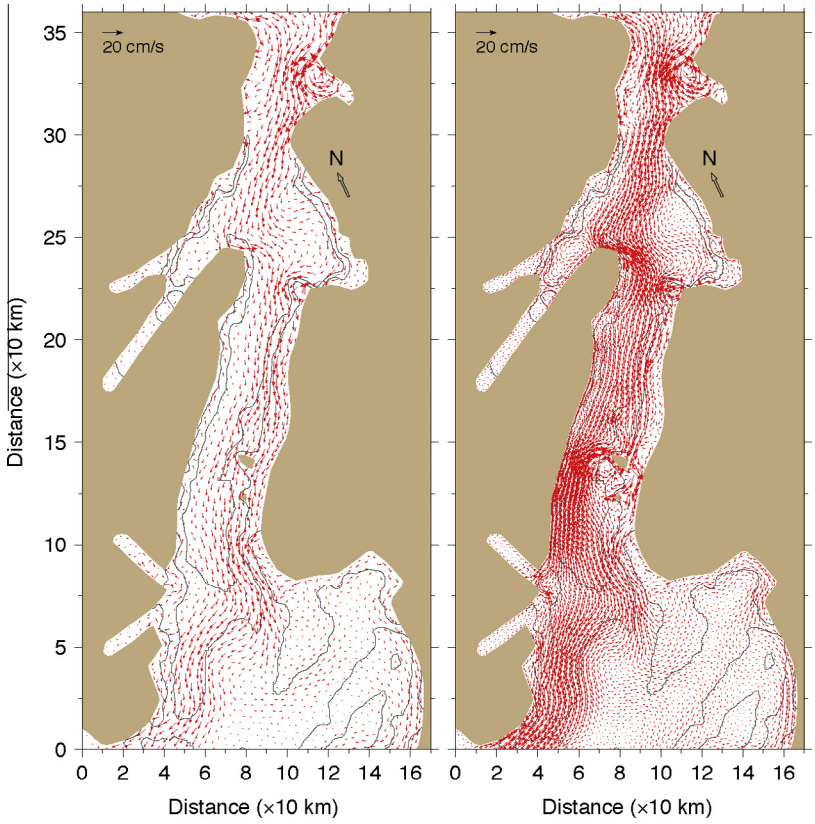

Fig. 8. Model-predicted annual-mean currents (red vectors) averaged over the upper 50-m water column in Nares Strait for the Grid-II case with the resolutions of 5 km (left) and 2 km (right), respectively. The velocity vectors displayed in both panels were spaced every 15 km apart. The arrow with "N" indicates the direction to the North Pole. (For interpretation of the references to colour in this figure legend, the reader is referred to the web version of this article.)

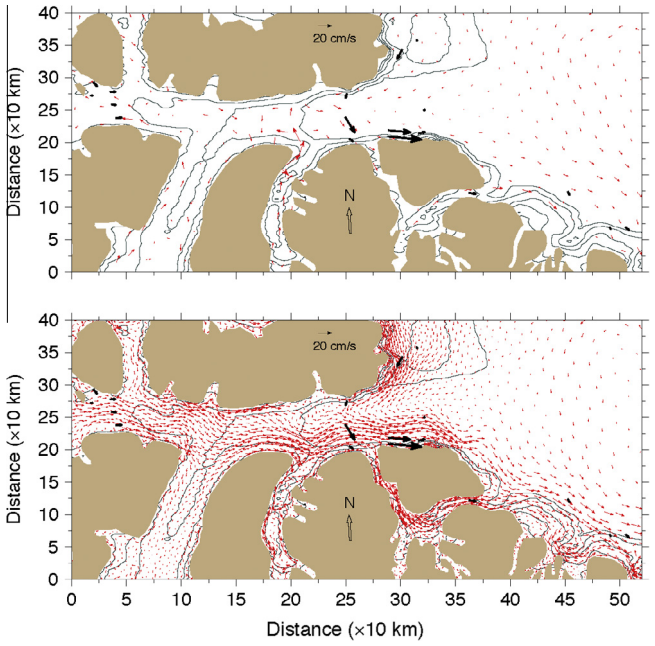

Fig. 9. Model-predicted annual-mean currents (red vectors) averaged over the upper 50-m water column in Lancaster Sound connected to Baffin Bay for the Grid-I (upper) and Grid-II (lower) cases. The observed velocities (black vectors) averaged annually and through the upper 50 m (when the multi-depth measurements were made) are superposed on the model field. The velocity vectors displayed in the Grid-II case are spaced every 15 km apart. The arrow with "N" indicates the direction to the North Pole. (For interpretation of the references to colour in this figure legend, the reader is referred to the web version of this article.)

Table 6
Volume and freshwater fluxes through Nares Strait.

Sources	Volume flux (Sv)	Freshwater flux (mSv)	Comments
AO-FVCOM (Grid-I: ~10 km)	−0.18	−6.2	1978–1994 climatology
AO-FVCOM (Grid-II: 5 km)	0.5	17.4	1978–1994 climatology
AO-FVCOM (Grid-II: 2 km)	0.5	17.5	1978–1994 climatology
Kiilerich (1939)	0.5		
Sadler (1976)	0.7 ± 0.1		April–June, 1972
Münchow et al. (2006)	0.8 ± 0.3	25.0 ± 12.0	August, 2003
Münchow et al. (2007)	0.91 ± 0.1	31.0 ± 4.0	August 2–14, 2003
Münchow and Melling (2008)	0.6 ± 0.1		Aug. 2003 to Aug. 2006
Rabe et al. (2012)	0.5 ± 0.1	20.0 ± 3.0	Geostrophic flux for 2003 and 2006

Note: The number within brackets in the top three rows is the finest resolution in the AO-FVCOM in Nares Strait.

between 7.5 km and 24 km was stronger on the right side than on the left side (Fig. 8: right panel). When the horizontal resolution was reduced to ~5 km (~0.5 R_I), this cross-strait flow pattern reversed (Fig. 9: left panel), even though this produced a similar volume flux through the strait (Table 6). When the resolution was 10 km, it even produced a northward net volume flux of ~−0.18 Sv, in the opposite direction to the observations (Table 6). In this coarse-resolution case, the initial water temperature and salinity were almost uniform across the strait. Since sea ice covered

this region during most of the year except in summer, the model failed to establish cross-shelf temperature and salinity gradients and thus the southward coastal jet current observed in field measurements. The observed net southward volume flux averaged over 2003–2006 through Nares Strait was ~0.6 ± 0.1 Sv (Münchow and Melling, 2008), with a large value of 0.8 ± 0.1 Sv occurring in August of 2003 (Münchow et al., 2006). Large variation appeared in the results based on shorter-term current measurements (e.g., Münchow et al., 2007; Sadler, 1976). The estimate based on geostrophic flux over 2003–2006 was 0.5 ± 0.1 Sv (Rabe et al., 2010, 2012). The model-predicted net southward volume flux was 0.5 Sv for Grid-I and 0.48 Sv for Grid-II, which was in good agreement with the observed flux estimated over multi-year measurements within the measurement uncertainty. The model-predicted net southward freshwater flux was 17.4 mSv for Grid-I and 17.5 mSv for Grid-II, which reasonably matched the observed flux of 20.0 ± 3.0 mSv estimated based on a multi-year hydrographic calculation within measurement uncertainty. This suggests that the grid resolution played a key role in capturing the shelf-strait current shear in the Canadian Archipelago, but the transport could be simulated reasonably in the case with a model resolution of ~0.5 R_I across the strait.

The importance of model resolution in the Canadian Archipelago can be also seen in Fig. 9, which shows the model-data comparison of the upper 50-m averaged flow in Lancaster Sound connected to Baffin Bay for the Grid-I and Grid-II cases. In Lancaster Sound, the grid resolution was ~20 km for Grid-I and ~9 km for Grid-II. The observations showed a well-defined anticyclonic flow of ~10–30 cm/s around the exit of Lancaster Sound. The spatial pattern, distribution and intensity of this flow were captured in the Grid-II case but were too weak in the Grid-I case (Fig. 9). The observations also showed an eastward outflow in the upstream area of this sound, which was captured in the Grid-II case, but the currents predicted by the Grid-I case flowed in the opposite direction.

Region IV – the Greenland and Labrador Sea shelf refers here to as the southern shelf of Greenland and the western-southern shelf of the Labrador Sea characterized with a sharp deep slope between the 1000–2000-m isobaths over a distance of 30–50 km (Fig. 10), a key pathway of the water transport from the Arctic Ocean to the northwestern Atlantic shelf. Both coarse- and refined-grid AO-FVCOMs showed a well-defined cyclonic slope current with a magnitude of up to 30 cm/s in the upper 100 m, flowing southward and then westward along the Greenland slope, splitting into two branches over the bifurcation area of deep bathymetry around the 2000- and 3000-m isobaths, and continuing to flow southward and then southeastward along the 1000–2000-m isobaths and between the 2000–3000-m isobaths over the western and southern slopes of the Labrador Sea (Fig. 10). The grid resolution in this region was ~25–50 km for Grid-I and ~5–15 km for Grid-II, respectively.

Better resolution of the slope in Grid-II produced a stronger flow between the 2000- and 3000-m isobaths over the western slope of the Labrador Sea and an intensified along-isobath flow near the northwestern Atlantic coast. Superimposing available observed current vectors upon the model-predicted, vertically-averaged flow field in the upper 100 m, the spatial distributions and magnitudes of the observed and model-predicted velocities were similar. We collected a total of 19 time series records of the velocity at moorings with measurement depths in a range of 10–150 m, and compared the velocities averaged over each time series with model-predicted, vertically-averaged velocity in the upper 150 m. For the Grid-I case, the mean values of the difference were 7.2 cm/s in flow speed and 41.8° in flow direction. The root-mean squared error (RMSE) was 9.0 cm/s in flow speed and 59.1° in flow direction. For the Grid-II case, the mean values of the difference

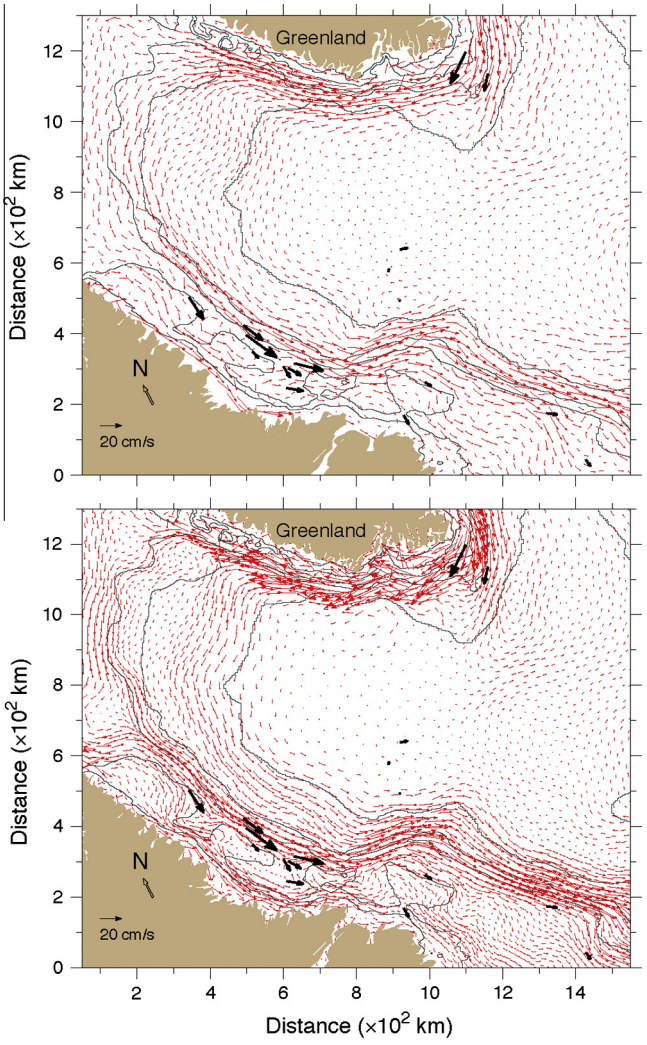

Fig. 10. Model-predicted annual-mean currents (red vectors) averaged over the upper 100-m water column over the Greenland and Labrador Sea shelves for the Grid-I (upper) and Grid-II (lower) cases. The observed velocities (black vectors) averaged annually and through the upper 100 m (when the multi-depth measurements were made) were superposed on the model field. The velocity vectors displayed in the Grid-II case are spaced every 15 km apart. The arrow with "N" indicates the direction to the North Pole. (For interpretation of the references to colour in this figure legend, the reader is referred to the web version of this article.)

were 5.9 cm/s in speed and 36.7° in direction. The RMSE of the flow direction was also reduced to 52.9°. Similar to Bering and Fram Straits, the direction error also varied with respect to the magnitude of the observed flow (Fig. 11); larger in the weak flow regime and smaller in the strong flow regime. It seemed like the refined grid model results were better. However, since the measurements were made in different years, at different water depths and at the same or close sites where intermittent time series records were available, the variability of the velocity in each time series over different measurement periods could be up to 18–20 cm/s, the model-data comparison results should be interpreted with caution.

Region V – the North Atlantic Ocean/Greenland Sea was partially included in the AO-FVCOM computational domain. Although our focus was on the Arctic Ocean, the model-data comparison in the North Atlantic Ocean provided us insights into the capability of this model to capture the basin-scale circulation that is directly relevant to the inflow and outflow of the Arctic Ocean. An annually averaged float-derived velocity field at a depth of 700-m depth in the subpolar region of the North Atlantic Ocean was constructed

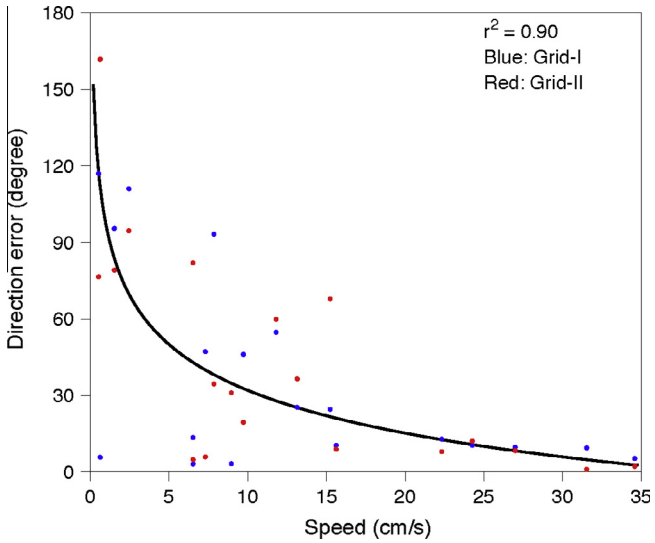

Fig. 11. Distribution of the velocity direction error versus the observed velocity magnitude for the comparison shown in Fig. 10. Black line: the regression fitting curve with a correlation coefficient of $r^2 = 0.90$ and RMSE = 13.1°. The fitting was done using the Matlab cftool.

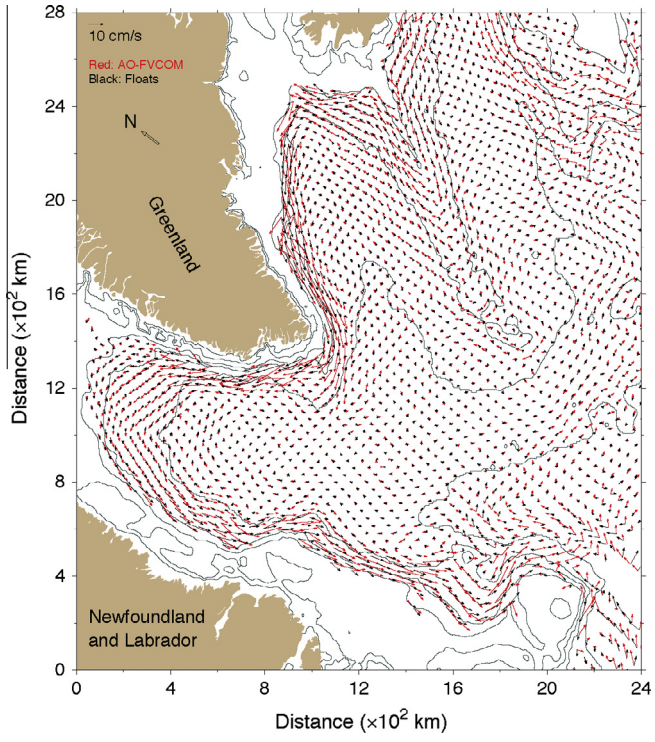

Fig. 12. Comparisons between model-predicted and float-derived annual mean velocities at a depth of 700 m in the North Atlantic Ocean/Greenland Sea. Black: float-derived; red: the Grid-II AO-FVCOM-derived. The arrow with "N" indicates the direction to the North Pole. (For interpretation of the references to colour in this figure legend, the reader is referred to the web version of this article.)

and published by Lavender et al. (2005). A total of 123 neutrally buoyant floats were deployed at a depth of 700 m in this region by the Woods Hole Oceanographic Institution (WHOI) and the resulting trajectory records covered the period from November 1994 to July 2002. The mean velocity was calculated by averaging all trajectory-derived velocities in a 25 × 25 km box over record lengths. Interpolating the Grid-II AO-FVCOM-computed velocity to nodes where float-derived velocities were calculated, we compared model-computed and observed velocities. AO-FVCOM captured the distribution of the slope current, the mid-depth cyclonic circulation over the deep slope, and the northeastward North Atlantic Drift Current (NADC) that were well resolved in the float-derived velocity field (Fig. 12). The mean values of the difference and RMSE were 3.8 and 6.2 cm/s in speed and 30.3° and 56.9° in direction. The mean speed of the float-derived cyclonic deep-slope circulation was ~7.0 cm/s, with a maximum up to ~19.0 cm/s. Considering that the uncertainty of the spatial-time average in the mean float-derived velocity exceeded 5 cm/s in the under-sampled areas (Lavender et al., 2005), the model-computed velocity was robust. The direction error was consistent with the measurement uncertainty: largest in the weakly flow regime of <5 cm/s and smaller in the strongly flow regime (Fig. 13). Statistics showed that 59% of samples showed a zero direction error. Dividing the direction errors into 10°-intervals, 60% of samples showed the direction error of <10°. Although 13% of samples had a direction error of >90°, they were mainly in the weakly flow regime where the velocity was within the measurement uncertainty.

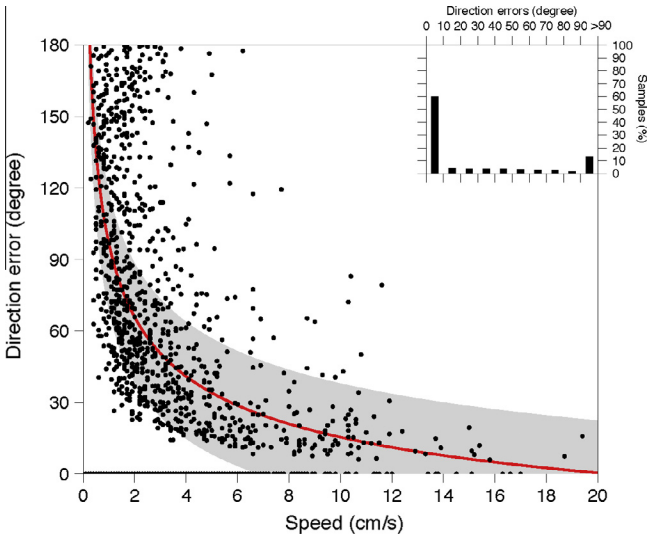

Fig. 13. Distribution of the velocity direction error versus the observed velocity magnitude for the comparison shown in Fig. 12. Red line: the regression fitting curve with a correlation coefficient of $r^2 = 0.98$ and RMSE = 7.6°; gray shaded area: the 95% confidence bounds of the regression fit; upper-right panel: the distribution (%) of measurement samples versus direction errors. (For interpretation of the references to colour in this figure legend, the reader is referred to the web version of this article.)

We also compared AO-FVCOM-computed velocity with float-derived flow at a depth of 1500 m, which also showed the same level of agreement as that at the 700-m level (Gao, 2011). The spatial distribution of the model-predicted velocity was in agreement with previous measurements made by Lazier and Wright (1993).

4. Discussion

4.1. Impacts of grid resolution on the slope currents

The Arctic Ocean is characterized by the slope cyclonic flow and the key to capture this flow relies on whether or not a model can resolve the steep bottom slope topography. In the Arctic Basin, where the cross-isobath scale of topography change over the slope is the same as the internal Rossby deformation scale, the failure to resolve slope topography can be equivalent to misrepresenting the dynamical scale of the motion and thus lead to an unrealistic flow pattern. A clear example can be seen in Fig. 14, which shows the

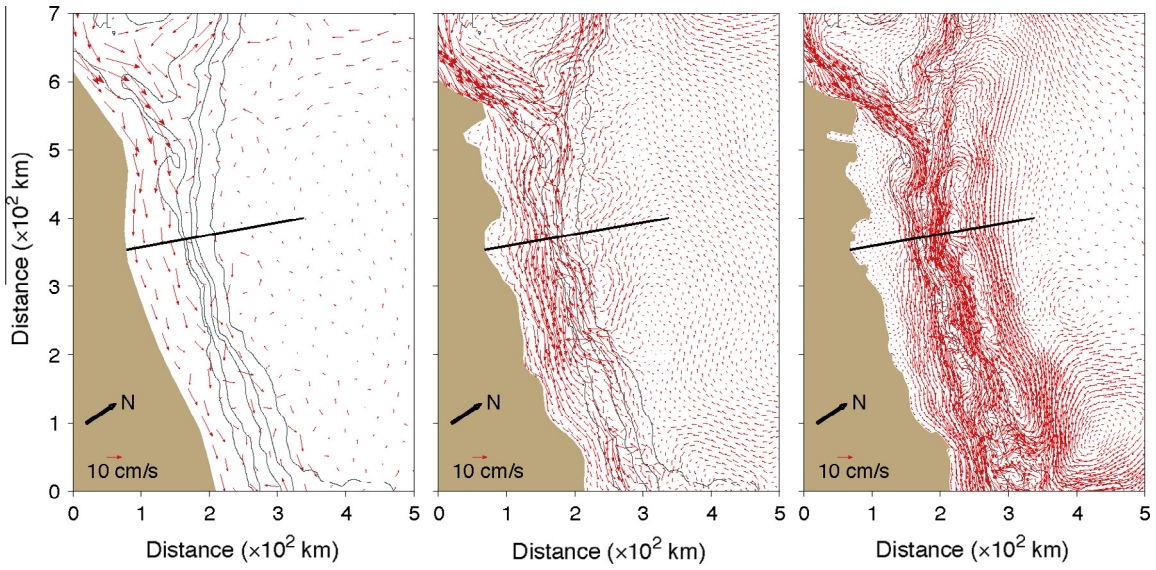

Fig. 14. Model-predicted annual-mean currents (red vectors) averaged over the upper 50-m water column over the Alaska shelf for the Grid-I (left), Grid-II (middle) and Grid-III (right) cases. The velocity vectors displayed in the Grid-II and Grid-III case are spaced every 15 km apart. The arrow with "N" indicates the direction to the North Pole. (For interpretation of the references to colour in this figure legend, the reader is referred to the web version of this article.)

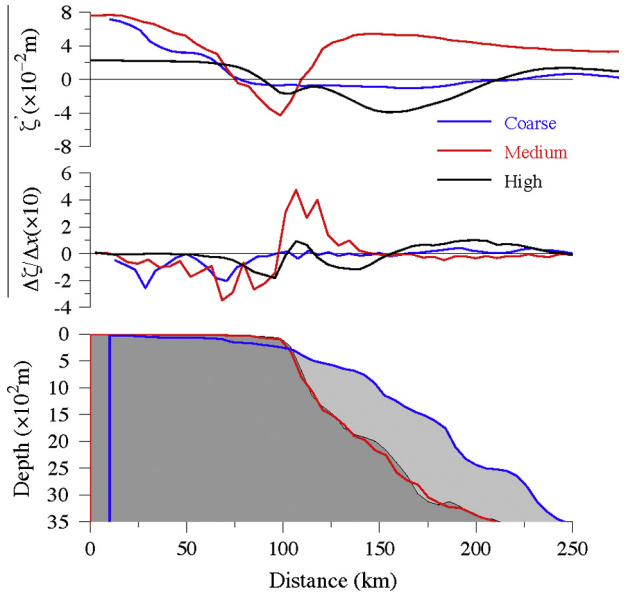

Fig. 15. Model-predicted annual anomaly sea levels relative to the section mean ($\zeta' = \zeta - \bar{\zeta}$) (top) and cross-shelf gradients of the surface elevation (middle) over the section (bottom) shown in Fig. 10. Blue: Grid-I; red: Grid-II, black: Grid-III. (For interpretation of the references to colour in this figure legend, the reader is referred to the web version of this article.)

comparison of the annually averaged flow field simulated by AO-FVCOM over the Alaska shelf for Grid-I, Grid-II, and Grid-III. The horizontal resolutions over this shelf were up to ~20–30 km, ~8–10 km and ~1 km for these three cases, respectively. Although these three cases all resolved the southward along-shelf flow, the cross-shelf distribution of this flow changed significantly with model resolution (Fig. 14). In the Grid-I case, the slope bottom topography was significantly smoothed; narrowing the width of the continental shelf and overestimating the bottom slope in the coastal region. As a result, the flow was coast-intensified and no strong slope current existed. In the Grid-II case, the slope bottom topography was reasonably resolved, the location of the maximum southward flow shifted offshore to form a current jet over the continental shelf close to the steep bottom slope. As horizontal resolution increased up to ~1 km in the Grid-III case, the current jet shifted to the slope with the appearance of complex mesoscale eddies.

The cross-shelf bottom topography along the section marked in Fig. 14 is shown in Fig. 15. The bottom depth changes from 100 m to 1000 m over a cross-shelf distance of ~10 km, with a slope of ~0.09. This slope was resolved in the Grid-II and Grid-III cases, but was over-smoothed in the Grid-I case. In the Grid-I case, the cross-shelf distance between the 100-m and 1000-m isobaths was ~80 km, which resulted in the smaller slope of ~0.01. In turn, the distance from the coast to the 100 m isobath was reduced, resulting in an overestimation of the bottom slope. Assuming that the along-shelf flow is in a semi-geostrophic balance, the cross-shelf distribution of the sea surface elevation changed significantly as the model resolution changed (Fig. 15). In the Grid-I case, the sea level had the maximum value at the coast and decreased offshore, which produced the coast-intensified southward flow. When the bottom topography was reasonably resolved in the Grid-II, the maximum sea level gradient shifted offshore, even though the cross-shelf distribution of the sea level remained similar to the Grid-I case. As the resolution increased to ~1 km in the Grid-III case, the sea level became relatively flat near the coast and reached a maximum around the slope. In this case, the model produced a well-defined southward current jet and also eddy-induced reverse flow over the slope.

The cross-shelf distribution of the model-simulated annually-averaged density significantly differed in the Grid-I, Grid-II and Grid-III cases. A near-surface density front appeared in the Grid-II and Grid-III cases over the continental shelf, but was not found in the Grid-I case (Fig. 16). The coarse resolution used in the Grid-I case did not resolve the near-shore area, resulting in a deeper water depth at the coast. In this case, the model-simulated isopycnals were relatively flat near the coast and then gradually deepened with water depth. At a given depth, the density decreased offshore. Refining the grid in the Grid-II case produced a shallower and wider shelf with a mean water depth of ~5 m at the coast. In this case, the model-simulated isopycnals over the continental shelf exhibited an opposite cross-shelf distribution

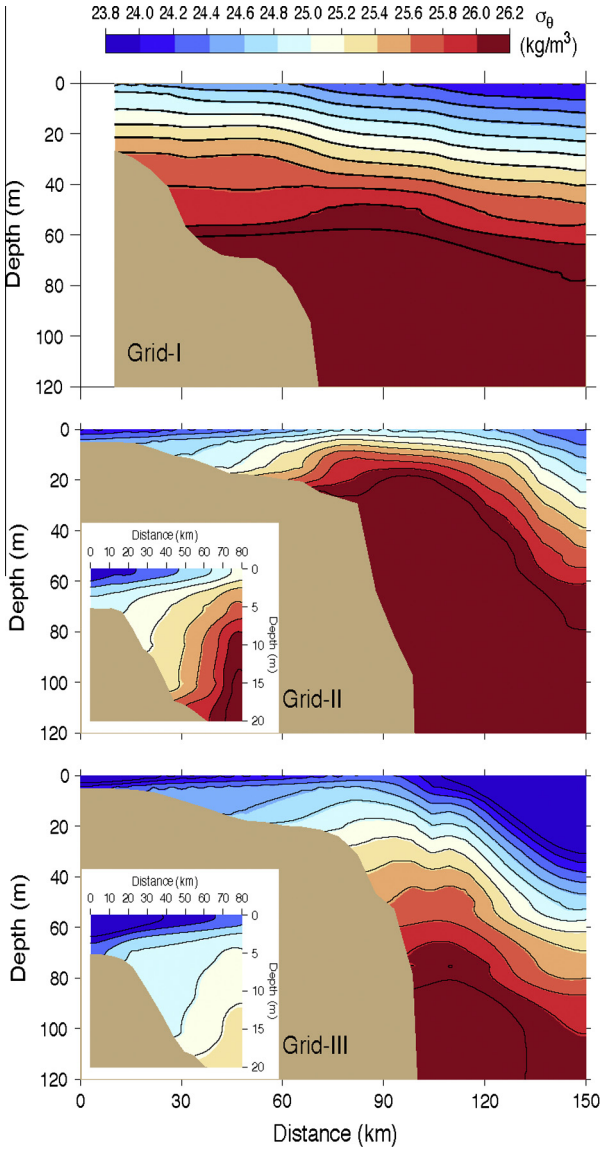

Fig. 16. Cross-shelf distributions of the annually averaged density simulated by the AO-FVCOM on the section marked in Fig. 14 for the Grid-I (top), Grid-II (middle) and Grid-III (bottom) cases. The figures inserted in the left-lower corners of middle and bottom panels provide an enlarged view of the density distribution in the upper 20 m over the shelf.

pattern, with the density increasing offshore. As the grid resolution was refined from the Grid-II case to the Grid-III case, the density exhibited the same cross-shelf distribution pattern, with strengthening of the cross-shelf density gradient. Over the slope where the mean water depth was greater than 150 m, the density featured an offshore-deepening of isopycnals, with the cross-shelf gradient increasing as the grid resolution was refined. This feature suggested that the anticyclonic reversed current over the outer edge of the slope was a stratified flow. Under the same surface forcing condition, the model-simulated density gradient over the shelf can be significantly influenced by the model resolution.

Greenberg et al. (2007) reviewed the need for adequate horizontal resolution regarding both tidal and subtidal current simulations. The criterion for the tidal motion was given as

$$\Delta x \leqslant \frac{T\sqrt{gH}}{n} \tag{2}$$

where T is the tidal period; g is the gravity; H is the mean water depth; and n is the number of nodes per wavelength. Based on Le Provost et al.'s (1995) analysis, n = 30 for the global tidal simulation. We included 8 semi-diurnal and diurnal tidal constituents in the simulation. Taking the M_2 tidal constituent (T = 12.42 h), H = 200 m (at the shelf break along the Alaska shelf), we have

$$\Delta x \leqslant 66 \text{ km}. \tag{3}$$

Therefore, the grid resolution used for the Grid-I, Grid-II and Grid-III cases in the AO-FVCOM was sufficient to resolve the tidal motion over the slope. Even in the near-coastal region (e.g., H = 10 m and $\Delta x \leqslant$ 15 km), the grid resolutions for all these cases were also sufficient.

For the subtidal flow, the dynamics over the slope are controlled by a cross-shelf motion scale defined as $H/\nabla H$ (Loder, 1980; Greenberg et al., 2007). On an assumption of steady state and no along-isobath variation, Greenberg et al. (2007) derived this scale through the continuity equation, which was given as

$$\frac{\partial U}{\partial x} \sim -\frac{1}{H}\frac{dH}{dx}U = -\alpha U. \tag{4}$$

For non-dimensional scaling, it yielded

$$\frac{U}{L_x} \sim -\alpha U \Rightarrow L_x \sim \frac{1}{\alpha} = \frac{H}{\nabla H} \tag{5}$$

where L_x is the cross-shelf motion scale and $\alpha = 1/HdH/dx$. Using a numerical model to produce an analytically-derived barotropic slope current, Hannah and Wright (1985) concluded that in order to reasonably reproduce this flow, the model resolution (Δx) must satisfy the criterion given as

$$\Delta x \leqslant 0.33\frac{H}{\nabla H} = 0.33L_x, \tag{6}$$

which is one-third of the cross-shelf motion scale. Applying this criterion for the subtidal flow over the slope of the Arctic Ocean where the topographic slope is ~0.01–0.02 on the 200-m isobath at the shelfbreak and ~0.1 on the 1000-m isobaths at the deep slope, we have

$$\Delta x \leqslant 3.3 - 6.6 \text{ km (at the shelf break)}$$
$$- 2 \text{ km (over the deep slope)}.$$

This is the resolution required to resolve the cross-shelf motion scale of the Arctic Ocean slope current. In our case, the Grid-III resolution satisfied this criterion, while the Grid-I resolution was at least three times larger. On the selected section, the Grid-II resolution was slightly larger than this criterion at the shelf break, but insufficient over the deep slope.

In addition to the requirement in resolving the cross-shelf motion scale, our experiments for the Grid-I, Grid-II and Grid-III cases showed that in the Grid-I case, the coarse resolution produced a much smoothed slope bottom topography with a greater gradient near the coast. As a result, the flow was coastally intensified and no strong slope current jet appeared. The along-shelf current jet appeared in the Grid-II case as the horizontal resolution was increased to ~8 km. The cross-shelf scale of this jet was significantly narrowed in the Grid-III case as the horizontal resolution improved to ~1 km over the slope. An offshore shifting of the current jet towards the shelf break with increasing grid resolution implied that in addition to the cross-shelf motion scale, resolving the topographic slope is critically important to simulate the location of this current jet.

Under barotropic conditions, we extended Greenberg et al. (2007)s analysis with the vorticity conservation theory assuming semi-geostrophic dynamics. The results of this analysis showed that the cross-shelf gradient of the surface elevation (ζ) can be given as

$$\frac{\partial \zeta}{\partial x} = -\frac{1}{R^2}\int_{x_o}^{x}(H - H_0)dx \tag{7}$$

where R is the Rossby deformation radius defined as $\sqrt{gH_o}/f$. Non-dimensional scaling yields

$$\Delta\zeta \sim \left(\frac{L_x}{R}\right)^2 \Delta H. \quad (8)$$

In addition to resolve the cross-shelf scale L_x, the cross-shelf change of the surface elevation is proportional to the change of the cross-shelf bottom topography. Even under a nonlinear condition that the along-shelf velocity is not semi-geostrophic and the cross-shelf advection flux cannot be ignored, we could derive a similar relationship to (8), in which the along-shelf velocity is proportional to the change of bottom topography. In the Grid-I case, the cross-shelf topographic gradient was exaggerated over the continental shelf but significantly underestimated over the slope. As a result, the surface elevation gradient had its maximum at the coast, producing a coastally-intensified structure of the along-shelf current. Grid refinement in the Grid-II and Grid-III cases provided a better resolution of the bathymetry change over the shelf and slope, which shifted the maximum cross-shelf gradient of the surface elevation towards the shelfbreak and thus produced a weak along-shelf flow near the coast.

Our results for the three cases clearly showed that the slope current over the continental shelf in the Arctic Ocean was a wind- and buoyancy-driven flow. In the Grid-II and Grid-III cases, the formation and intensity of this flow was companied with the cross-shelf density front. The cross-shelf scale of this density front was estimated based on a simple 1.5 layer model, which equals the internal Rossby deformation radius (R_l) given as

$$L_x \sim R_l = \frac{\sqrt{g'H}}{f} \quad (9)$$

where g' is the reduced gravity defined as $g(\rho_2 - \rho_1)/\bar{\rho}$; g is the gravity; ρ is the density; subscripts "1 and 2" represents layers 1 and 2, respectively, and superscript " – " is the sign for the mean value. Here R_l is the baroclinic motion scale. In the Grid-II and Grid-III cases, R_l for the density front over the shelf was ~5–8 km. Following a similar approach used in Hannah and Wright (1985) to resolve this baroclinic density frontal structure, one requires a horizontal resolution to satisfy

$$\Delta x \leqslant 0.33R_l \sim 1.7 - 2.6 \text{ km}.$$

Our experiments suggested that when the model was capable of resolving the bottom slope, it produced the shelf-intensified southward flow. To resolve the slope-intensified flow, the model required a resolution capable of resolving the dominant dynamics within the internal Rossby deformation scale. The resolution had a direct impact on the reality of the surface elevation and baroclinic pressure gradient simulation, which differed from the eddy-slope interaction-induced lateral diffusion process described in the Neptune Theory.

The Grid-II and Grid-III were capable of resolving this baroclinic scale, while Grid-I failed. Of most importance is to resolve both the cross-shelf topographic scale of $H/\nabla H$ (Loder, 1980; Greenberg et al., 2007) and the density front scale defined by R_l. On the section selected in Fig. 14, the resolutions required to resolve the bottom slope and baroclinic density front were equivalent, so that when one of either conditions was satisfied, the model was capable of resolving the slope current over that shelf.

The change in the spatial distribution of the slope flow with model resolution had a direct impact on the volume transport from the Arctic Basin to the CAA. In Section 4, we reported that in Nares Strait, the coarse resolution used in the Grid-I case produced a northward transport in opposition to observations. A further analysis was conducted to examine how the flux into the CAA was influenced due to the change of the slope flow with grid resolution.

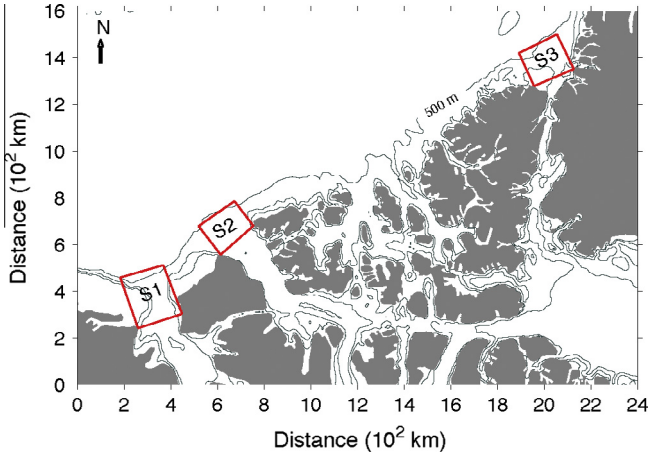

Fig. 17. Locations of the selected closed boxes (S1, S2 and S3) for the estimation of the volume transport into the CAA for the Grid I, Grid-II and Grid-III cases.

Three closed boxes, named sites S1, S2 and S3, were selected in this analysis (Fig. 17), and the volume transport into the CAA was estimated by calculating the transport into or out of each section of the box. At site S1, the transport into the CAA was −0.35 Sv in the Grid-I case, but decreased to −0.08 Sv and −0.05 Sv in the Grid-II and Grid-III cases, respectively (Fig. 18: top panel). It is clear that the offshore shifting of the along-shelf current with grid refinement tended to reduce the transport into that CAA strait. In this box, the shelf and upstream sections featured inflow. The change of the cross-shelf transport on these two sections directly affected the outflow into the CAA and on the downstream section. At site S2, an opposite tendency was found, which showed that the transport into the CAA increased with grid refinement, with values of −0.12 Sv in the Grid-I case, −0.22 Sv in the Grid-II case, and −0.30 Sv in the Grid-III case (Fig. 18: mid-panel), respectively. In this box, in all three cases, the inflow transport was only from the upstream section, while the other sections featured outflow. The maximum change in inflow transport was ~12% among these three cases, but the change of outflow transport was up to ~68% on the shelf section, ~60% on the CAA section, and ~41% on the downstream section. At site S3, the volume flux into the CAA (Nares

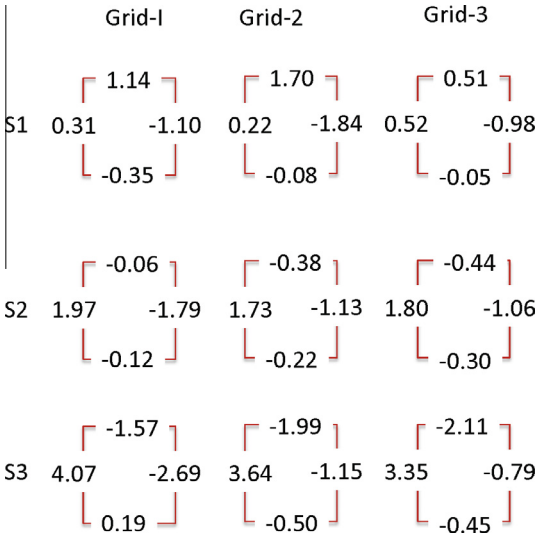

Fig. 18. Volume transport through each section of boxes S1, S2 and S3 for the Grid I, Grid-II and Grid-III cases. On each box, top: the shelf section; left: the upstream section; right: the downstream section, and bottom: the CAA section. Unit: Sv.

Strait) in the Grid-I case had an opposite sign compared with the Grid-II and Grid-III cases (Fig. 18: bottom panel). The inflow transport on the upstream section decreased with grid refinement, with a maximum difference accounting for ~18% of the flux in the Grid-I case. In the Grid-II and Grid-III cases, the shelf, downstream and CAA sections were all featured by the outflow transport. The inflow transport on the upstream section dropped from 3.64 Sv to 3.35 Sv (about a 8% difference) when the Grid-III was used to replace the Grid-II. Correspondingly, the outflow transport was decreased by 31% and 10% on the downstream and CAA sections, respectively, and increased by 6% on the shelf section. The Grid-I case produced a greater inflow transport on the upstream section, which was ~22% greater compared with the Grid-III case. On the downstream section, the outflow transport in the Grid-I case was 3.41 times as large as the flux in the Grid-III case, although the outflow transport on the shelf section was ~26% less. These differences resulted in the outflow flux from the CAA, which showed an opposite sign to observed transports. In summary, by influencing the isobaths that the mean flow follows, the resolution over the slope in the Arctic Ocean imposes important controls over the magnitude and spatial distribution of the flows through the CAA.

4.2. Cyclonic slope flow and topostrophy

In the upper 50 m, the AO-FVCOM showed that the annually-averaged currents in the Arctic Basin were dominated by the wind- and ice-drifting-driven anticyclonic circulation, but over the slope, the flow was cyclonic (Fig. 19: upper panel). In the 200–600-m depth layer, the model produced a well-defined annually-averaged cyclonic slope flow (Fig. 19: lower panel). This flow entered the Arctic over the slope off Svalbard through Fram Strait, streamed and turned cyclonically along the slope of the continental shelf and moved out of the Arctic along the slope of Greenland through Fram Strait. The model-simulated cyclonic slope flow in both the 50-m and 200–600-m layers was a permanent feature, since the standard deviation of this flow only accounted for 15% and 12% of the total kinetic energy in these two upper and deep layers, respectively.

A complex empirical orthogonal function (EOF) analysis was used to investigate the spatial and temporal variability of the Arctic Ocean circulation. The algorithm used in this method was described in Kundu and Allen (1976) and Brink and Muench (1986) with the updated additional references of Salstein et al. (1983), Hannachi et al. (2007) and Sun (2014). Whether or not normalizing or de-trending the time series in the EOF analysis really depends on the goal one tried to pursue. For the case in which the mean was dominant, the EOF analysis without de-trending the mean could help us to examine the absolute fluctuation of the dominant signal. An example was given by Salstein et al. (1983). In our case, we found that the cyclonic slope flow was a dominant feature. We first conducted the EOF analysis without removal of the annual-mean value and examined if the dominant cyclonic flow was a year-around feature. In both the upper and deep layers, we found that the flow-fields produced by the first mode, which accounted for 85% and 88% of the total kinetic energy,

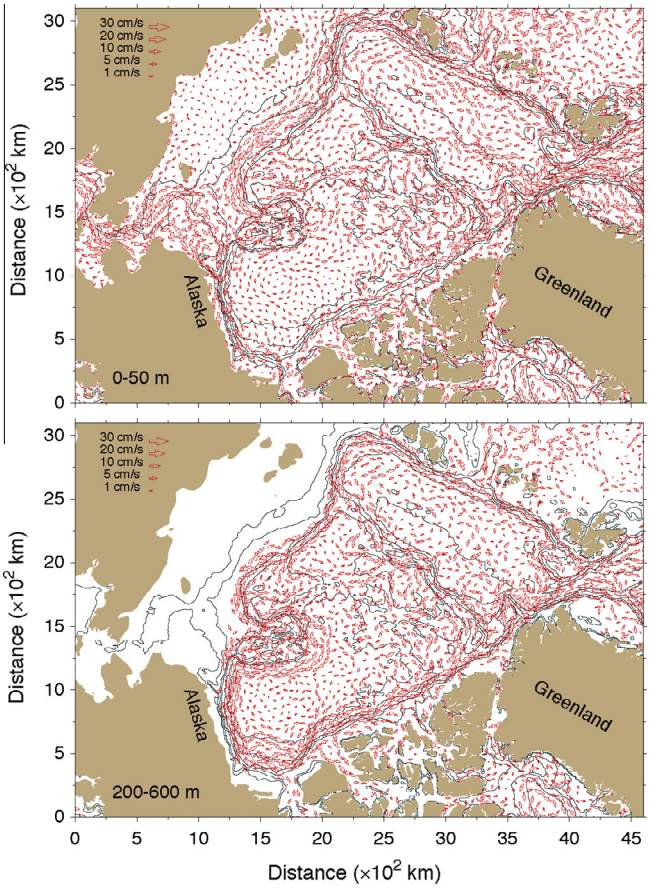

Fig. 19. Spatial distributions of the annually mean flow averaged through the upper 50-m water column (upper panel) and the deep 200–600-m water column (lower panel). The velocity vector is rescaled using the root-square scale and spaced 50 km apart.

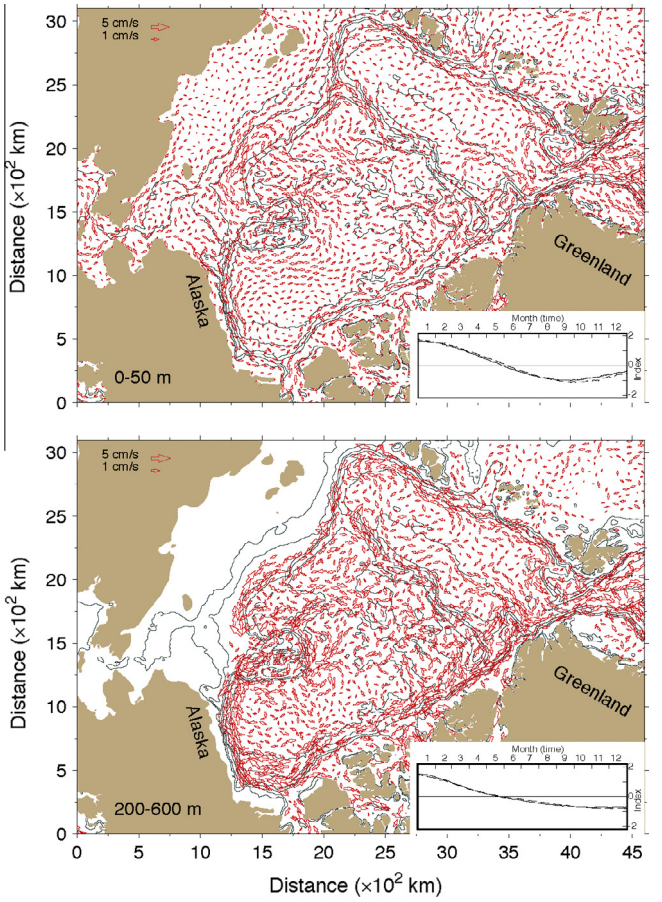

Fig. 20. Spatial distributions of the 1st EOF mode velocities averaged through the upper 50-m water column (upper panel) and the deep 200–600 m water column (lower panel). The figure inserted in the right-lower area of each panel presents the temporal variation of the 1st EOF mode velocity. The velocity vector is rescaled using the root-square scale and spaced 50 km apart.

respectively. This result was very similar to the annual-mean flows shown in Fig. 19. We also found that the temporal variation of the 1st-mode-derived flow remained positive, indicating that the cyclonic slope flow a stable and relative year-around feature. To examine the temporal variability of the Arctic circulation, we removed the annual mean velocity at individual cells and re-conducted the EOF analysis. In the upper 50-m and 200–600-m layers, the 1st–5th EOF modes accounted for 45.6% and 58.0%; 30.3% and 20.9%; 9.9% and 10.6%; 4.2% and 4.5%; and 2.1% and 1.7% of the total variance, respectively. The 1st and 2nd EOF modes were predominant, which accounted for 75.9% and 78.9% of the total variance in the upper and deep layers, respectively.

In both the upper and deep layers, the 1st EOF mode exhibited semi-annual variations: positive in January–May and negative in July–December with a sign change in early June (Fig. 20). The 2nd EOF mode provided a view of the seasonal variation, negative in January–February, positive in April–August, and negative again in October–December, with sign transitions in March and September, respectively (Fig. 21). The spatial distributions of the flow derived from the 1st and 2nd EOF modes were very complex (Figs. 20 and 21). In general, the variation was larger over the slope than in the interior basin. Even in the same flow system, the variation significantly varied in space. An example can be seen in the 1st mode flow field in the upper 50-m layer, where the flow direction over the slope of the continental shelf connected to the CAA was opposite to that over the slope of Alaska and other regions. It should be noticed that the EOF analysis was conducted based on the daily averaged velocity field of a year, in which the semi-annual variation is the longest resolvable variation scale. The maximum magnitude of the spatial and temporal variations derived by a sum of 1st and 2nd modes was about 5–6 cm/s over the slope and ~1.0 cm/s or less in the interior basin. These values were the same as the standard deviation of the flow relative to the annual mean.

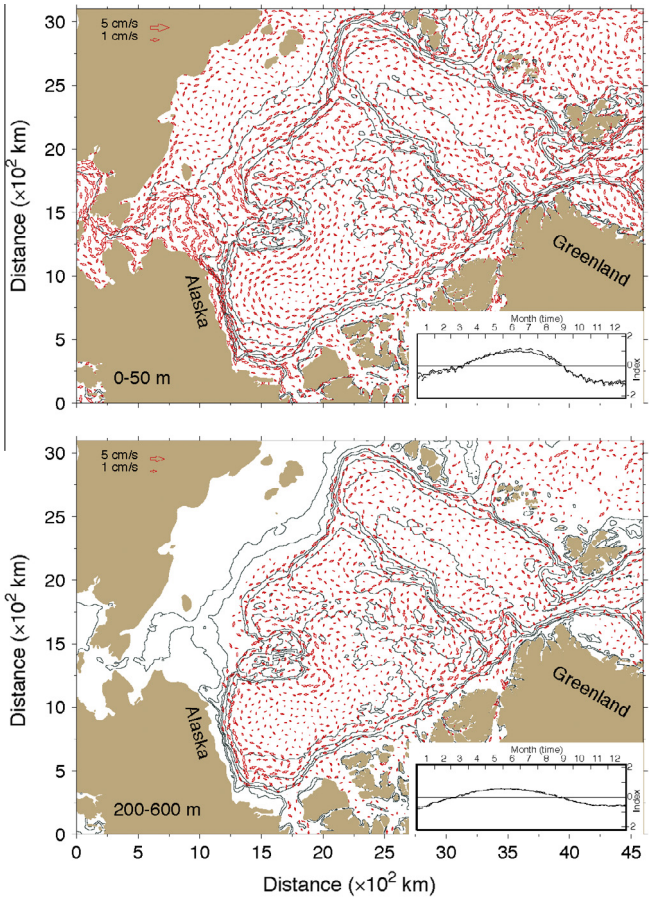

Fig. 21. Spatial distributions of the 2nd EOF mode velocities averaged through the upper 50-m water column (upper panel) and the deep 200–600 m water column (lower panel). The figure inserted in the right-lower area of each panel presents the temporal variation of the 2nd EOF mode velocity. The velocity vector is rescaled using the root-square scale and spaced 50 km apart.

Consistent with observations, the AO-FVCOM-predicted currents in the deep 200–600-m layer in the Arctic Ocean were characterized by a large positive topostrophy value over the slope (Fig. 22). The cross-slope gradient of this value varied with model grid resolution, particularly in the narrow shelf region with a width of ~100 km along the western coast of the Beaufort Sea and northern coast of the Canadian Archipelago. The mesoscale variability of topostrophy increased as the model grid resolution was refined, which is consistent with the dynamical interpretation for the comparison shown in Fig. 10. The normalized value of topostrophy averaged in the entire Arctic Ocean, defined as $\langle (1/A \iint \tau dA)|\tau_{max}| \rangle$ where the sign "$\langle\rangle$" represented the mean over a year, was 0.83 in both the Grid-I and Grid-II cases (Fig. 23). As the resolution around the western shelf of the Beaufort Sea was improved to ~1.0 km (Grid-III), numerous mesoscale eddies were produced along the cyclonic slope flow. Since these eddies were mainly restricted in the deep side of the slope, the Arctic Basin was still characterized by a large positive topostrophy with a normalized mean value of ~0.55 (Fig. 23). The time variability of the normalized topostrophy relative to its mean value was in a range of −0.1 to 0.15 in the Grid-I case. As the model resolution was refined, the variability increased in magnitude, with a value from −0.2 to 1.5 in the Grid-II case and from −0.2 to 0.43 in the Grid-III case. Nine models were selected for AOMIP, in which three models with inclusion of a Neptune term produced a positive topostrophy value of ~0.6–0.65, but the other six models failed to produce a large positive topostrophy (Holloway and Wang, 2009). For those three Neptune models, the temporal variability of normalized topostrophy was in a maximum range of 0.1 or less. Both the mean and variability were significantly smaller than those shown in Grid-I, Grid-II and Grid-III AO-FVCOM simulations that do not include the Neptune terms.

4.3. Sensitivity of flux calculation to sampling resolutions

The Arctic Ocean is a basin where the water transport is controlled by the inflow from Bering Strait and net outflow through Fram Strait and the Canadian Archipelago. The Bering Strait is the only passageway in the Arctic that opens to the Pacific Ocean. The flow there was dominated by the inflow from the Pacific to the Arctic and the magnitude of the flow in the strait did not change significantly as resolution increased from Grid-I to Grid-III. The difference found in the volume flux was mainly due to the change of the section area value in different resolutions. The Fram Strait contains both the North Atlantic inflow along and around Svalbard and the Arctic outflow along the Greenland shelf. In this inflow-outflow strait, a net volume flux value could be sensitive to sampling resolution in both the horizontal and vertical.

We conducted a sensitive study by resampling the model-predicted velocity on an across-strait section with a horizontal resolution from 4 to 28 km and a vertical resolution from 10 to 45 layers (Fig. 24). The model results used for this experiment were from the Grid-III case in which the model resolution was ~4 km in the horizontal and 45 layers in the vertical. The linear interpolation method was used for both the horizontal and vertical. If only the horizontal resolution was considered, no well-defined monotonic function with respect to resolution existed. In this case, the mean volume flux ($\overline{V}_m$) obtained from seven sampling resolutions was −2.0 Sv with a standard deviation of 0.2, and a maximum

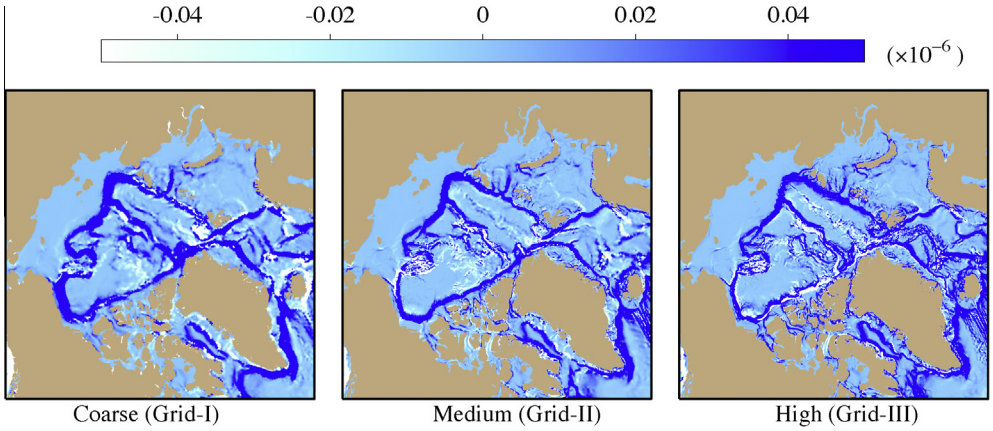

Fig. 22. Topostrophies calculated by the model-predicted flow fields for the Grid-I (left), Grid-II (middle) and Grid-III (right) cases.

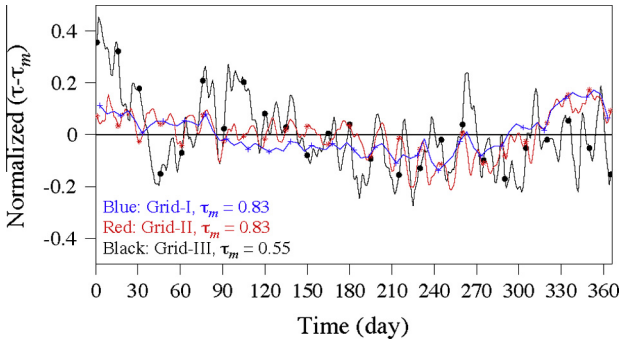

Fig. 23. Normalized topostrophy values averaged over the entire Arctic region defined by Bering Strait on the Pacific Ocean side and Fram Strait on the North Atlantic Ocean side for the Grid-I (blue), Grid-II (red) and Grid-III (black) cases. τ is the normalized topostrophy and τ_m is the annual mean of τ. (For interpretation of the references to colour in this figure legend, the reader is referred to the web version of this article.)

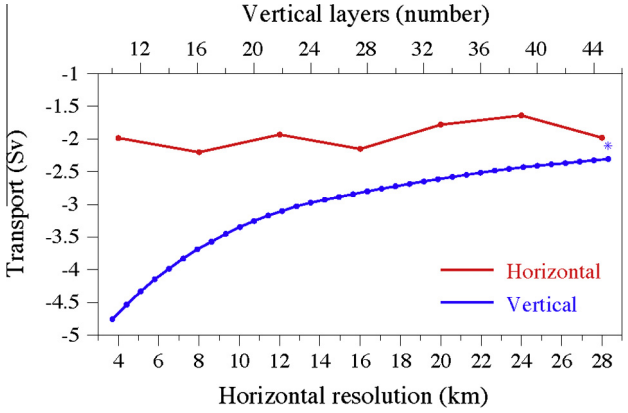

Fig. 24. Net volume transports versus horizontal resolution (red line) and vertical resolution (blue line) across Fram Strait. The asterisk symbol is the flux estimated with the 45 non-uniform layers configured by the hybrid vertical coordinate used in AO-FVCOM. The resampling experiments were made using the Grid-III AO-FVCOM results. (For interpretation of the references to colour in this figure legend, the reader is referred to the web version of this article.)

difference up to 0.6 Sv. The ratio of $(V_i - \overline{V}_m)$ to $\overline{V}_m$ (V_i is the volume flux obtained for the ith resampling) varied in a range of 1.0–16.0%, while the corresponding ratio for the section areas varied only in the range of 0.1–0.8%. This suggested that the flux difference in various horizontal resolution cases was caused by under-sampling the mesoscale flow field across the strait. The net volume flux could be influenced significantly by the vertical sampling resolution. When 10 layers were considered, the model predicted a net volume flux of ~4.9 Sv. The flux monotonically decreased as vertical sampling resolution increased. When 45 layers were used, the net volume flux was ~2.3 Sv. The difference in the flux obtained from 10 and 45 layers reached 2.5 Sv. This suggested that it is critical to resolve the vertical shear of the velocity in the strait in order to obtain a reasonable estimate of the net volume flux. It should be noted here that the flux listed in Table 5 was estimated based on 45 non-uniform hybrid model layers, while the flux for 45 layers shown above was estimated by interpolated uniform layers. The difference between these two methods can be ~0.2 Sv.

This sensitivity analysis results suggested that the changes in the systematic errors in the observational estimates of the transports in Fram Strait could be caused by the change of the horizontal and vertical resolutions of the observations over the years. Particular attentions should be paid on this issue when the interannual variability of the flux through Fram Strait is studied based on the flux estimated from the observations with various spatial sampling resolutions in different years.

5. Summary

Built on the success in developing a high-resolution, unstructured-grid global-regional nested ice-current coupled FVCOM system for the Arctic Ocean, we have examined the impact of model resolution and geometrical fitting on the basin-coastal scale circulation and the volume and salt fluxes entering and flowing out of the Arctic region. Without the need to invoke the Neptune theory, AO-FVCOM was capable of resolving multi-scale circulations in the Arctic, including cyclonic slope flow, inflow through Bering Strait, a strong shear in the inflow and outflow in Fram Strait, and outflow through the CAA. Our numerical model results showed that in order to resolve the shelf-intensified cyclonic slope flow, the model resolution must be capable of resolving both the cross-shelf topographical and baroclinic density frontal scales. To resolve the slope-intensified flow over the continental shelf and coastal-intensified current in narrow straits and water passages, the model needs to have a cross-slope resolution capable of resolving the physical scale defined by the internal Rossby deformation radius. The resolution had a direct impact on both the reality of the simulation of the surface elevation and baroclinic pressure gradient and thus the structure of the current over the slope, and the accuracy of the flux from the Arctic Basin to the CAA.

The AO-FVCOM was capable of reproducing the general circulation patterns in the Arctic Ocean. In the upper 50-m layer, the

wind- and ice-drifting-driven anticyclonic circulation dominated the interior basin and the cyclonic slope flow prevailed over the continental shelf. In the deep 200–600-m layer, the circulation featured a well-defined annually averaged cyclonic slope flow. The model-produced temporal variation of the flow was dominated by the 1st and 2nd EOF modes, which accounted for 15% and 12% of the total kinetic energy in these upper and deeper layers. Consistent with observations, the AO-FVCOM-predicted cyclonic slope flow was characterized by a large positive topostrophy value over the slope. The cross-slope gradient of this value varied significantly with grid refinement: increasing as grid resolution improved.

The estimation of the net volume flux entering and out of the Arctic Ocean can also be influenced by sampling resolution. In Bering Strait, the flow was dominated by the inflow with its magnitude changing slightly with model resolution, i.e., the model-estimated net volume flux did not change significantly as the model resolution was increased. In Fram Strait, the flow was characterized by the strong lateral current shear between the Atlantic inflow and Arctic outflow, such that the net flux can change significantly as different sampling resolutions were chosen. It is critical to resolve the cross-strait variability and vertical shear of the mesoscale flow field in the design of the sampling resolution needed for an accurate estimation of the volume flux.

Since Holloway and Wang (2009)s work, many high-resolution models have been developed to resolve the complex multi-scale circulation in the Arctic Ocean. Aksenov et al. (2010) applied a *z*-coordinate global Ocean Circulation and Climate Advanced Model (OCCAM) to estimate the Arctic freshwater outflow. The OCCAM had a horizontal resolution up to 8.3 km, which was capable of resolving the cyclonic slope current like that described in the Grid-II result of AO-FVCOM. Houssais and Herbaut (2011) applied the NEMO (Nucleus for European Modelling of the Ocean) version 1.9 to examine the influence of the atmospheric forcing on the CAA outflow. This model had a horizontal resolution of 22 km in the Arctic Ocean, which was incapable of resolving the internal Rossby deformation radius in the CAA and geometry of narrow straits and water passages. McGeehan and Maslowski (2012) used the Naval Postgraduate School Arctic Modeling effort model (named NAME) to estimate the CAA outflow. This model had a horizontal resolution of ~9 km, which were similar to the Grid-II resolution used in AO-FVCOM. This model was capable of resolving the cyclonic slope current and providing a reasonable estimation of the CAA outflow transport through Nares Strait and Lancaster Sound. Wekerle et al. (2013) applied a global unstructured grid, *z*-coordinate Finite-Element Sea Ice-Ocean Model (FESOM) to simulate the CAA outflow transport. This model has a horizontal resolution up to 5 km in the CAA region. In Nares Strait, the horizontal resolution of FESOM was similar to the Grid-II resolution used in AO-FVCOM. Lu et al. (2014) applied the version 2.3 of NEMO to simulate the flux into the CAA. In their experiments, a resolution of 6 km was used in the horizontal, which was similar to FESOM used in Wekerle et al. (2013). As pointed out in our experiments, this resolution could provide a reasonable estimation of the outflow transport but it may not resolve the cross-strait structure of the outflow in Nares Strait and other narrow water passages. A detailed comparison of AO-FVCOM with FESOM, NAME and NEMO was given for the 1978–2013 hindcast simulation results in Zhang et al. (submitted for publication).

It should be noticed that under the climatological forcing conditions our experiments did resolve the Beaufort Gyre. The clockwise Beaufort Gyre appeared in both the upper 50-m and deep 200–600-m layers, but its spatial scale was significantly underestimated. Recently, we have run AO-FVCOM Grid-II for the period of 1978–2014. By checking the real-time simulation results, we found that the gyre exhibited a significant seasonal and interannual variation in magnitude and spatial scale. The Woods Hole Oceanographic Institution has established a long-term monitoring network in the Beaufort Sea. We collected the current measurement data at four sites for the period of 2003–2011. The vertically averaged velocity over the depth range of 69–199 m clearly showed a clockwise circulation with a magnitude of ~1 cm/s. AO-FVCOM was capable of producing the clockwise Beaufort Gyre with the same magnitude of the velocity as the observations, but the model-predicted and observed currents showed a significant difference in direction. An investigation of the influence of winds, ice formation/melting, and stratification on the temporal and spatial variability of the Beaufort Gyre is being conducted. Since this study used climatological forcing conditions, no comparisons of the observed currents with the real-time simulation from 1978 to 2013 are given here.

Acknowledgments

This work was supported by US National Science Foundation (NSF) Grants OCE-1203393 for the UMASSD team and PLR-1203643 for the WHOI team. The Global-FVCOM/AO-FVCOM system was developed with infrastructure support by the Sino-US Joint Innovative Center for Polar Ocean Research (SU-JICPOR), International Center for Marine Studies, Shanghai Ocean University. G. Gao was supported by the National Natural Science Foundation of China under Grant number 41276197, the Shanghai Pujiang Program under Grant number 12PJ1404100, and the Shanghai Shuguang Program. We would like to thank Dr. Andrey Proshutinsky for his valuable comments and suggestions and Dr. David Greenberg for sharing his square-root scale plotting program with us. Discussions with him during the AO-FVCOM development have really helped us improve our understanding of the Arctic Ocean circulation and recent model developments and improvement. Finally, the anonymous reviewers provided valuable and constructive suggestions that helped us clarify our scientific findings described in this paper.

References

Aagaard, K., Carmack, E.C., 1989. The role of sea ice and freshwater in the Arctic circulation. Journal of Geophysical Research 94, 14485–14498. http://dx.doi.org/10.1029/JC094iC10.

Aksenov, Y., Bacon, S., Coward, A.C., Holliday, N.P., 2010. Polar outflow from the Arctic Ocean: a high resolution model study. Journal of Marine Systems 83 (1), 14–37.

Barron, C.N., Smedstad, L.F., 2002. Global river inflow within the navy coastal ocean model. In: Proceedings, MTS/IEEE Ocean 2002 Conference, 29 October 2002, Biloxi, MS, pp. 1472–1479.

Brink, K.H., Muench, R.D., 1986. Circulation in the point conception-Santa Barbara Channel Region. Journal of Geophysical Research 91 (C1), 877–895.

Burchard, H., 2002. Applied Turbulence Modeling in Marine Waters. Springer, Berlin, Heidelberg, New York, Barcelona, Hong Kong, London, Milan Paris, Tokyo, pp. 215.

Chen, C., Liu, H., Beardsley, R.C., 2003. An unstructured, finite-volume, three-dimensional, primitive equation ocean model: application to coastal ocean and estuaries. Journal of Atmospheric and Oceanic Technology 20, 159–186.

Chen, C., Beardsley, R.C., Cowles, G., 2006a. An unstructured grid, finite-volume coastal ocean model (FVCOM) system. Special Issue entitled "Advances in Computational Oceanography". Oceanography 19 (1), 78–89.

Chen, C., Beardsley, R.C., Cowles, G., 2006b. An unstructured grid, finite-volume coastal ocean model-FVCOM user manual. School for Marine Science and Technology, University of Massachusetts Dartmouth, New Bedford, second ed. Technical Report SMAST/UMASSD-06-0602, pp. 318.

Chen, C., Huang, H., Beardsley, R.C., Liu, H., Xu, Q., Cowles, G., 2007. A finite-volume numerical approach for coastal ocean circulation studies: comparisons with finite difference models. Journal of Geophysical Research 112, C03018. http://dx.doi.org/10.1029/2006JC003485.

Chen, C., Gao, G., Qi, J., Proshutinsky, A., Beardsley, R.C., Kowalik, Z., Lin, H., Cowles, G., 2009. A new high-resolution unstructured-grid finite-volume Arctic Ocean model (AO-FVCOM): an application for tidal studies. Journal of Geophysical Research 114, C08017. http://dx.doi.org/10.1029/2008jc004941.

Chen, C., Beardsley, R.C., Cowles, G., Qi, J., Lai, Z., Gao, G., Stuebe, D., Liu, H., Xu, Q., Xue, P., Ge, J., Ji, R., Hu, S., Tian, R., Huang, H., Wu, L., Lin, H., Sun, Y., Zhao, L., 2013. An unstructured-grid, finite-volume community ocean model FVCOM

user manual (3rd ed.). SMAST/UMASSD Technical Report-13-0701, University of Massachusetts-Dartmouth, pp. 404.
Clement, J.L., Maslowski, W., Cooper, L.W., Grebmeier, J.M., Walczowski, W., 2005. Ocean circulation and exchanges through the northern Bering Sea-1979-2001 model results. Deep Sea Research II 52, 3509–3540.
Coachman, L.K., Aagaard, K., Tripp, R.B., 1975. Bering Strait: The Regional Physical Oceanography. University of Washington Press, Seattle, 172 pp.
Coachman, L.K., Aagaard, K., 1988. Transports through Bering Strait: annual and interannual variability. Journal of Geophysical Research 93 (C12), 15535–15539.
Dickson, R., Brown, J., 1994. The production of North Atlantic Deep Water: sources, rates and pathways. Journal of Geophysical Research 99 (C6), 12319–12341.
Dickson, R., Rudels, B., Dye, S., Karcher, M., Meincke, J., Yashayaev, I., 2007. Current estimates of freshwater flux through Arctic and subarctic seas. Progress in Oceanography 73, 201–230.
Eby, M., Holloway, G., 1994. Sensitivity of a large scale ocean model to parameterization of topographic stress. Journal of Physical Oceanography 24, 2577–2588.
Fahrbach, E., Meincke, J., Østerhus, S., Rohardt, G., Schauer, U., Tverberg, V., Verduin, J., 2001. Direct measurements of volume transports through Fram Strait. Polar Research 20 (2), 217–224.
Gao, G., 2011. An unstructured-grid finite-volume Arctic ICE-Ocean coupled model (AO-FVCOM: development, validation and applications. Ph.D. dissertation, University of Massachusetts School of Marine Sciences-Amherst-Boston-Dartmouth-Lowell-Worcester, 200 pp.
Gao, G., Chen, C., Qi, J., Beardsley, R.C., 2011. An unstructured-grid, finite-volume sea ice model: development, validation, and application. Journal of Geophysical Research 116, C00D04. http://dx.doi.org/10.1029/2010JC006688.
Greenberg, D.A., Dupont, F., Lyard, F.H., Lynch, D.R., Werner, F.E., 2007. Resolution issues in numerical models of oceanic and coastal circulation. Continental Shelf Research 27, 1317–1343.
Hannachi, A., Jolliffe, I.T., Stephenson, D.B., 2007. Review empirical orthogonal functions and related techniques in atmospheric science: a review. International Journal of Climatology 27, 1119–1152.
Hannah, C.G., Wright, D.G., 1985. Depth dependent analytical and numerical solutions for wind-driven flow in the coastal ocean. Coastal and Estuarine Studies 4, 125–152.
Holland, D.M., Mysak, L.A., 1996. An investigation of the general circulation of the Arctic Ocean using an isopycnal model. Tellus 48A, 138–157.
Holfort, J., Hansen, E., 2004. Report of the Freshwater Fluxes through Fram Strait (preliminary results). Report to ASOF-N 2004, 6pp mimeo +8 figs.
Holloway, G., Dupont, F., Golubeva, E., Hakkinen, S., Hunke, E., Jin, M., Karcher, M., Kauker, F., Maltrud, M., Morales Maqueda, M.A., Maslowski, W., Platov, G., Stark, D., Steele, M., Suzuki, T., Wang, J., Zhang, J., 2007. Water properties and circulation in Arctic Ocean models. Journal of Geophysical Research 112, C04S03. http://dx.doi.org/10.1029/2006JC003642.
Holloway, G., 2008. Observing global ocean topostrophy. Journal of Geophysical Research 113, C07054. http://dx.doi.org/10.1029/2007JC004635.
Holloway, G., Wang, Z., 2009. Representing eddy stress in an Arctic Ocean model. Journal of Geophysical Research 114, C06020. http://dx.doi.org/10.1029/2008JC005169.
Houssais, M.N., Herbaut, C., 2011. Atmospheric forcing on the Canadian Arctic Archipelago freshwater outflow and implications for the Labrador Sea variability. Journal of Geophysical Research 116 (C8), C00D02. http://dx.doi.org/10.1029/2010JC006323.
Hunke, E.C., Lipscomb, W.H., 2006. CICE: The Los Alamos sea ice model documentation and software user's manual. Report, Los Alamos Natl. Lab., Los Alamos, N.M.
Ingvaldsen, R., Asplin, L., Loeng, H., 2004. The seasonal cycle in the Atlantic transport to the Barents Sea during the years 1997–2001. Continental Shelf Research 24, 1015–1032.
Karcher, M.J., Oberhuber, J.M., 2002. Pathways and modification of the upper and intermediate waters of the Arctic Ocean. Journal of Geophysical Research 107 (C6), 3049. http://dx.doi.org/10.1029/2000JC000530.
Karcher, M., Gerdes, R., Kauker, F., Köberle, C., Yashayaev, J., 2005. Arctic Ocean change heralds North Atlantic freshening. Geophysical Research Letters 32, L21606. http://dx.doi.org/10.1029/2005GL023861.
Kiilerich, A.B., 1939. The Godthaab Expedition 1928 – a Theoretical Treatment of the Hydrographical Observation Material. Medd. Grønland 78 (5), 1–148.
Kobayashi, M.H., Pereira, J.M.C., Pereira, J.C.F., 1999. A conservative finite-volume second-order-accurate projection method on hybrid unstructured grids. Journal of Computational Physics 150, 40–45.
Kundu, P.K., Allen, J.S., 1976. Some three-dimensional characteristics of low-frequency current fluctuations near the Oregon coast. Journal of Physical Oceanography 6, 181–199.
Lavender, K.L., Owens, W.B., Davis, R.E., 2005. The mid-depth circulation of the subpolar North Atlantic Ocean as measured by subsurface floats. Deep Sea Research Part I – Oceanographic Research Papers 52, 767–785.
Lazier, J.R.N., Wright, D.G., 1993. Annual velocity variations in the Labraador Current. Journal of Physical Oceanography 23, 659–678.
Le Provost, C., Cenco, M.L., Lyard, F., 1995. Modeling and predicting tides over the world ocean. In: Lynch, D.R., Davies, A.M. (Eds.), Quantitative Skill Assessment for Coastal Ocean Models, Coastal and Estuarine Series, vol. 47. American Geophysical Union, Washington, DC, pp. 75–201.
Loder, J.W., 1980. Topographic rectification of tidal currents on the sides of Georges Bank. Journal of Physical Oceanography 10, 1399–1416.
Lu, Y., Higginson, S., Nudds, S., Prinsenberg, S., Garric, G., 2014. Model simulated volume fluxes through the Canadian Arctic Archipelago and Davis Strait: linking monthly variations to forcing in different seasons. Journal of Geophysical Physics 119, 1927–1942. http://dx.doi.org/10.1002/2013JC009408.
Maslowski, W., Marble, D., Walczowski, W., Schauer, U., Clement, J.L., Semtner, A.J., 2004. On climatological mass, heat, and salt transports through the Barents Sea and Fram Strait from a pan-Arctic coupled ice-ocean model simulation. Journal of Geophysical Research 109, C03032. http://dx.doi.org/10.1029/2001JC001039.
McGeehan, T., Maslowski, W., 2012. Evaluation and control mechanisms of volume and freshwater export through the Canadian Arctic Archipelago in a high-resolution pan-Arctic ice-ocean model. Journal of Geophysical Research 117 (C8). http://dx.doi.org/10.1029/2011JC007261.
Mellor, G.L., Yamada, T., 1982. Development of a turbulence closure model for geophysical fluid problem. Review of Geophysical Space Physics 20, 851–875.
Meredith, M., Heywood, K., Dennis, P., Goldson, L., White, L.R., Fahrbach, E., Schauer, U., Østerhus, S., 2001. Freshwater fluxes through the western Fram Strait. Geophysical Research Letters 28 (8), 1615–1618.
Münchow, A., Melling, H., Falkner, K., 2006. An observational estimate of volume and freshwater flux leaving the Arctic Ocean through Nares Strait. Journal of Physical Oceanography 36, 2025–2041.
Münchow, A., Falkner, K., Melling, H., 2007. Spatial continuity of measured seawater and tracer fluxes through Nares Strait, a dynamically wide channel bordering the Canadian Archipelago. Journal of Marine Research 65, 759–788.
Münchow, A., Melling, H., 2008. Ocean current observations from from Strait to west of Greenland: interannual to tidal variability and forcing. Journal of Marine Research 66, 801–833.
Proshutinsky, A., Steele, M., Zhang, J., Holloway, G., Steiner, N., Hakkinen, S., Holland, D., Gerdes, R., Koeberle, C., Karcher, M., Johnson, M., Maslowski, W., Walczowski, W., Hibler, W., Wang, J., 2001. Multinational effort studies differences among Arctic Ocean models. Eos, Transactions American Geophysical Union 82 (51), 637. http://dx.doi.org/10.1029/01EO00365.
Rabe, B., Münchow, A., Johnson, H.L., Melling, H., 2010. Nares Strait hydrography and salinity field from a 3-year moored array. Journal of Geophysical Research 115, C07010. http://dx.doi.org/10.1029/2009JC005966.
Rabe, B., Johnson, H.L., Münchow, A., Melling, H., 2012. Geostrophic ocean currents and freshwater fluxes across the Canadian Polar shelf via Nares Strait. Journal of Marine Research 70, 603–640.
Roach, A.T., Aagaard, K., Pease, C.H., Salo, S.A., Weingartner, T., Pavlov, V., Kulakov, M., 1995. Direct measurements of transport and water properties through the Bering Strait. Journal of Geophysical Research 100, 18443–18457.
Rudels, B., Marnela, M., Eriksson, P., 2008. Constraints on estimating mass, heat and freshwater transports in the Arctic Ocean: an exercise. In: Dickson, R.R. et al. (Eds.), Arctic-Subarctic Ocean Fluxes, pp. 315–341.
Rudels, B., 2011. Volume and freshwater transports through the Canadian Arctic Archipelago-Baffin Bay system. Journal of Geophysical Research 116, C00D10. http://dx.doi.org/10.1029/2011JC007019.
Sadler, H.E., 1976. Water, heat and salt transports through Nares Strait, Ellesmere Island. Journal Fishery Research Board Canada 33, 2286–2295.
Salstein, D.A., Rosen, R.D., Peixoto, J.P., 1983. Modes of variability in annual hemispheric water vapor and transport fields. Journal of the Atmospheric Science 40, 788–802.
Schauer, U., Fahrhach, E., Østerhus, S., Gerd, R., 2004. Arctic warming through the Fram Strait: oceanic transport from 3 years of measurements. Journal of Geophysical Research 109, C06026. http://dx.doi.org/10.1029/2004JC001823.
Schauer, U., Beszczynska-Möller, A., Walczowski, W., Fahrbach, E., Piechura, J., Hansen, E., 2008. Variation of measured heat flow through the Fram Strait between 1997 and 2006. In: Dickson, R.R. et al. (Eds.), Arctic-Subarctic Ocean Fluxes, pp. 65–85.
Smagorinsky, J., 1963. General circulation experiments with the primitive equations, I. The basic experiment. Monthly Weather Review 91, 99–164.
Sun, Y., 2014. Long- and Short-term Oceanic Responses to Atmospheric Forcing over the Gulf of Maine and New England Shelf. Ph.D dissertation, University of Massachusetts, 225 pp.
Steele, M., Morley, R., Ermold, W., 2001. PHC: A global ocean hydrography with a high quality Arctic Ocean. Journal of Climate 14, 2079–2087. http://dx.doi.org/10.1175/1520-0442.
Weingartner, T.J., Cavalieri, D.J., Aagaard, K., Sasaki, Y., 1998. Circulation, dense water formation, and outflow on the northeast Chukchi shelf. Journal of Geophysical Research 103, 7647–7661.
Weingartner, T., Aagaard, K., Woodgate, R.A., Danielson, S., Sasaki, Y., Cavalieri, D., 2005. Circulation on the north central Chukchi Sea shelf. Deep Sea Research II 52, 267–288. http://dx.doi.org/10.1016/j.dsr2.2005.10.015.
Wekerle, C., Wang, Q., Danilov, S., Jung, T., Schröter, J., 2013. The Canadian Arctic Archipelago throughflow in a multiresolution global model: model assessment and the driving mechanism of interannual variability. Journal of Geophysical Research 118 (9). http://dx.doi.org/10.1002/jgrc.20330.
Woodgate, R.A., Aagaard, K., 2005. Revising the Bering Strait freshwater flux into the Arctic Ocean. Geophysical Research Letters 32, L02602. http://dx.doi.org/10.1029/2004GL021747.
Woodgate, R.A., Aagaard, K., Swift, J.H., Falkner, K.K., Smethie, J.W.M., 2005a. Pacific ventilation of the Arctic Ocean's lower halocline by upwelling and diapycnal mixing over the continental margin. Geophysical Research Letters 32, L18609. http://dx.doi.org/10.1029/2005GL023999.
Woodgate, R.A., Aagaard, K., Weingartner, T., 2005b. Monthly temperature, salinity, and transport variability of the Bering Strait throughflow. Geophysical Research Letters 32, L04601. http://dx.doi.org/10.1029/2004GL021880.

Woodgate, R.A., Aagaard, K., Weingartner, T.J., 2006. Interannual changes in the Bering Strait fluxes of volume, heat and freshwater between 1991 and 2004. Geophysical Research Letters 33, L15609. http://dx.doi.org/10.1029/2006GL02693.

Woodgate, R.A., Weingartner, T.J., Lindsay, R.W., 2010. The 2007 Bering Strait oceanic heat flux and anomalous Arctic sea-ice retreat. Geophysical Research Letters 37, L01602. http://dx.doi.org/10.1029/2009GL041621.

Zhang, Y., Chen, C., Beardsley, R. C., Gao, G., Lai, Z., Curry, B., Lee, C. M., Lin, H., Qi, J., Xu, Q., 2014. Studies of the Canadian Arctic Archipelago outflow flux and its relationship to basin-local forcing: results from AO-FVCOM. Journal of Geophysical Research, submitted for publication.